TSPM Site Description

Code: TEC/TSPM-PDR/004

Issue: 1.B

Date: 2 October 2017

Pages: 44

Authors:	Michael Richer, David Urdaibay
Revised by:	
Approved by:	

Distribution List

Name	Affiliation

Document Change Record

Issue	Date	Section	Page	Change description
1A				Original issue.
1B		§6.2, §7.3, §6.2, §8.3, §6.1		General update and additional references. Adds (1) information from later versions of R.1, (2) information concerning atmospheric turbulence, (3) information concerning the vertical structure of the wind (R.15), (4) updated seismic design spectrum to 975 year return period and included example time series of the ground acceleration, (5) details concerning the temperature gradients near sunset.

Applicable and Reference Documents

Nº	Document Name	Code
R.1	Summary of wind measurements at the Observatorio Astronómico Nacional in the Sierra San Pedro Mártir	ANA/TSPM/001
R.2	Summary of temperature variations at the Observatorio Astronómico Nacional in the Sierra San Pedro Mártir	ANA/TSPM/002
R.13	Alvarez, M., & Maisterrena, J. 1977, RMxAA, 2, 43	
	Alvarez et al. 2007, RMxAAC, 31, 111	
	Avila et al. 2004, PASP, 116, 682	
	Avila et al. 1998, PASP, 110, 1106	
R.3	Bohigas, J., & Núñez, J. M. 2010, RMxAA, 46, 89	
R.6	Echevarria, J., et al. 1998, RMxAA, 34, 47	
	Falchi et al. 2016, Sci. Adv., 2, e1600377	
	Hiriart, D. 2003, RMxAA, 39, 119	
	Hiriart et al. 2003, RMxAAC, 19, 90	
R.10	López, J. A., & Gutiérrez, L. 2003, RMxAAC, 19, 3	
R.11	Michel et al. 2001, RMxAA, 37, 165	
R.12	Michel et al. 2003, RMxAAC, 19, 99	
R.14	Mendoza, E. E. 1971, Boll. Obs. Tac. Ton., 6, 95	
R.9	Otárola, A., et al. 2010, PASP, 122, 470	

	Otárola et al. 2009, RMxAA, 45, 161	
R.5	Plauchu-Frayn, I., et al. 2016, PASP, accepted	
R.8	Sánchez, L., et al. 2003, RMxAAC, 19, 23	
	Sánchez et al. 2008, PASP, 120, 1244	
	Schöck et al. 2009, PASP, 121, 384	
	Schuster, W. J., & Parrao, L. 2001, RMxAA, 37, 187	
	Schuster, W. et al. 2002, J. Ast. Data, 8, 2	
R.7	Skidmore, W., et al. 2009, PASP, 121, 1151	
	Tapia, M. 1992, RMxAA, 24, 179	
	Tapia, M. 2003, RMxAAC, 19, 75	
R.4	Tapia, M., et al. 2007, RMxAAC, 31, 47	
	Westphal, J. A. 1974, Infrared Sky Noise Survey, Final Report NASA Grant NGR 05-002-185, California Institute of Technology	
	Els, S. G., et al. 2009, PASP, 121, 527	
	Bohigas, J., et al. 2008, RmxAA, 44, 231	
R.15	The vertical structure of the wind at the OAN-SPM	ANA/TSPM/004

INDEX

1. SUMMARY

The site of the Observatorio Astronómico Nacional on the Sierra San Pedro Mártir (OAN-SPM) was chosen in the 1960's based upon the criteria that the site enjoy (1) a large number of clear nights, (2) dark skies, (3) low PWV, (4) good seeing, and (5) that it be located far from large urban areas (Mendoza 1971). After 45 years of experience at the site, experience shows that these criteria remain virtues of the OAN-SPM today. Presently, three telescopes are in operation, another is in commissioning, and three additional projects are under construction. All of the infrastructure to operate and maintain these telescopes exists on site. In the near future, the OAN-SPM will be connected to the national electricity grid and acquire a fibre optic communications connection at the same time. Both the climate and astroclimate are very favourable for a wide range of astronomical activities. In 2010, a state-wide lighting ordnance came into effect that should help maintain the skies in SPM dark. Recent geotechnical studies at the TSPM building site indicate that this site is very suitable for the project. These studies include a site specific seismic hazard analysis.

2. OBJECTIVE

The objective of this document is to familiarize the reader with the Observatorio Astronómico Nacional on the Sierra San Pedro Mártir (OAN-SPM) and with the particular site chosen for the Telescopio San Pedro Mártir (TSPM) project.

3. SCOPE

This document considers all aspects of the site: its location, the infrastructure present, the climate, the astroclimate, and its geologic and geophysical properties, including a site specific seismic hazard analysis. A summary of some of this information may be found in López & Gutiérrez (2003).

4. PHYSICAL LOCATION

The Sierra San Pedro Mártir (SPM) is the most recent of the locations that the Observatorio Astronómico Nacional (OAN) has occupied during its history (Figure 1). Previously, the OAN had been located in Mexico City, Tacubaya (now part of Mexico City), and Tonantzintla, in the state of Puebla. The Tonantzintla station of the OAN remains active. Although the OAN was established in the nineteenth century, its custody and maintenance was transferred to the Universidad National Autónoma de México (UNAM) in 1921 when the latter was given its autonomy. Since 1968, the OAN has been entrusted to the Instituto de Astronomía (IA-UNAM).

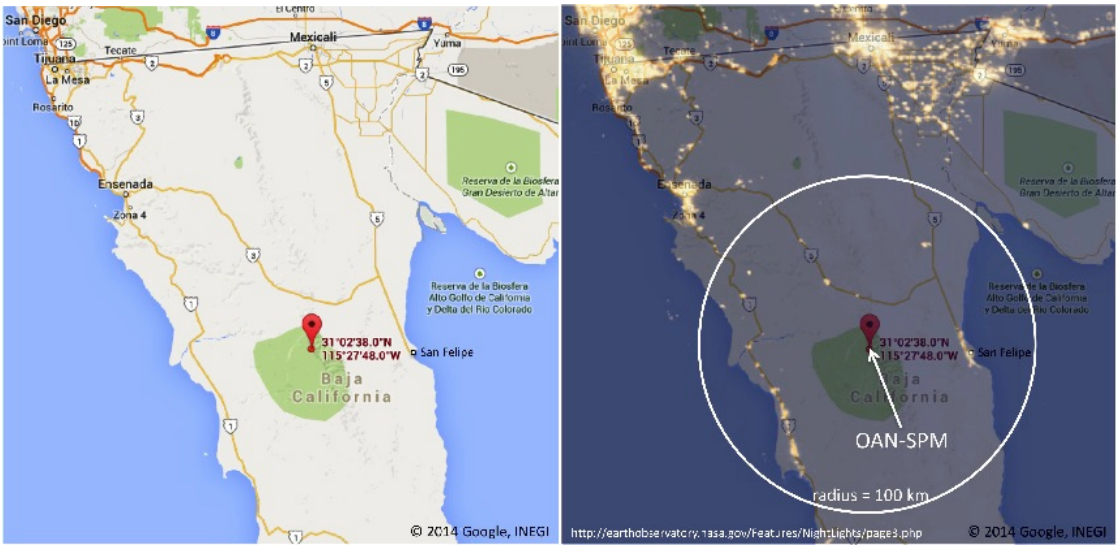

Figure 1: The OAN-SPM is located in the north central part of the state of Baja California, within the Parque Nacional Sierra de San Pedro Mártir (PNSSPM). Left: The Google Earth map of the area indicates the OAN-SPM's isolation from large urban areas. The only access to the OAN-SPM is via the transpeninsular highway 140 km south from Ensenada, then east 100 km on an access road that traverses the PNSSPM. Right: The area covering northern Baja California from the 2012 NASA Earth Observatory map of the Earth at night is superposed upon a Google Earth map of the same area, again emphasizing how remote the OAN-SPM is from urban areas. The marine layer regularly blocks the lights along the Pacific coast of the peninsula.

The site in SPM was chosen in the mid-1960s when it became clear that light pollution would impede further development of the OAN's installations in Tonantzintla. Given that this was not the first time this had happened, the decision was taken to find the location with the best weather for astronomy and the likelihood of evading serious light pollution for decades to come. Both criteria pointed to the mountain ranges running down the Baja California peninsula, the Sierra de Juárez and the Sierra San Pedro Mártir. The latter is the higher of the two and the OAN-SPM is located in the highest area of this mountain range, though not on its highest peak. The weather in northern Baja California was already known to be favorable (Mt. Palomar and Kitt Peak National Observatory are both "nearby"). SPM's distance from the cities on the US border and the aridity of the surrounding areas argued in favour of the skies remaining dark.

Site prospecting in the SPM area began in 1967. The first building and the 1.5m telescope at the OAN-SPM were finished in 1970. The headquarters of the OAN-SPM has been located in Ensenada during its entire history. Initially, the observatory headquarters were nearly exclusively administrative and technical, but the Instituto de Astronomía later established a research group in Ensenada that was eventually built into a complete research centre.

The OAN-SPM is 140 km southeast of Ensenada in a direct line of sight (see Figure 1) However, the distance by road is 240 km, first via the transpeninsular highway, then via the access road that

leads to the PNSSPM and the OAN-SPM. The latter access road had to be built in order to develop the OAN-SPM. This access road is paved along its entire length. Ensenada is the nearest shipping port to the OAN-SPM. The nearest commercial airports are in Tijuana and San Diego, California.

5. INFRASTRUCTURE

Figure 2 presents a map of the OAN-SPM. The installations are found in two groups. Near the entrance and at lower elevation is the support area. The telescopes are located on a higher ridge to the north of the support area. López & Gutiérrez (2003) present an overview of some of the results that follow in this section.

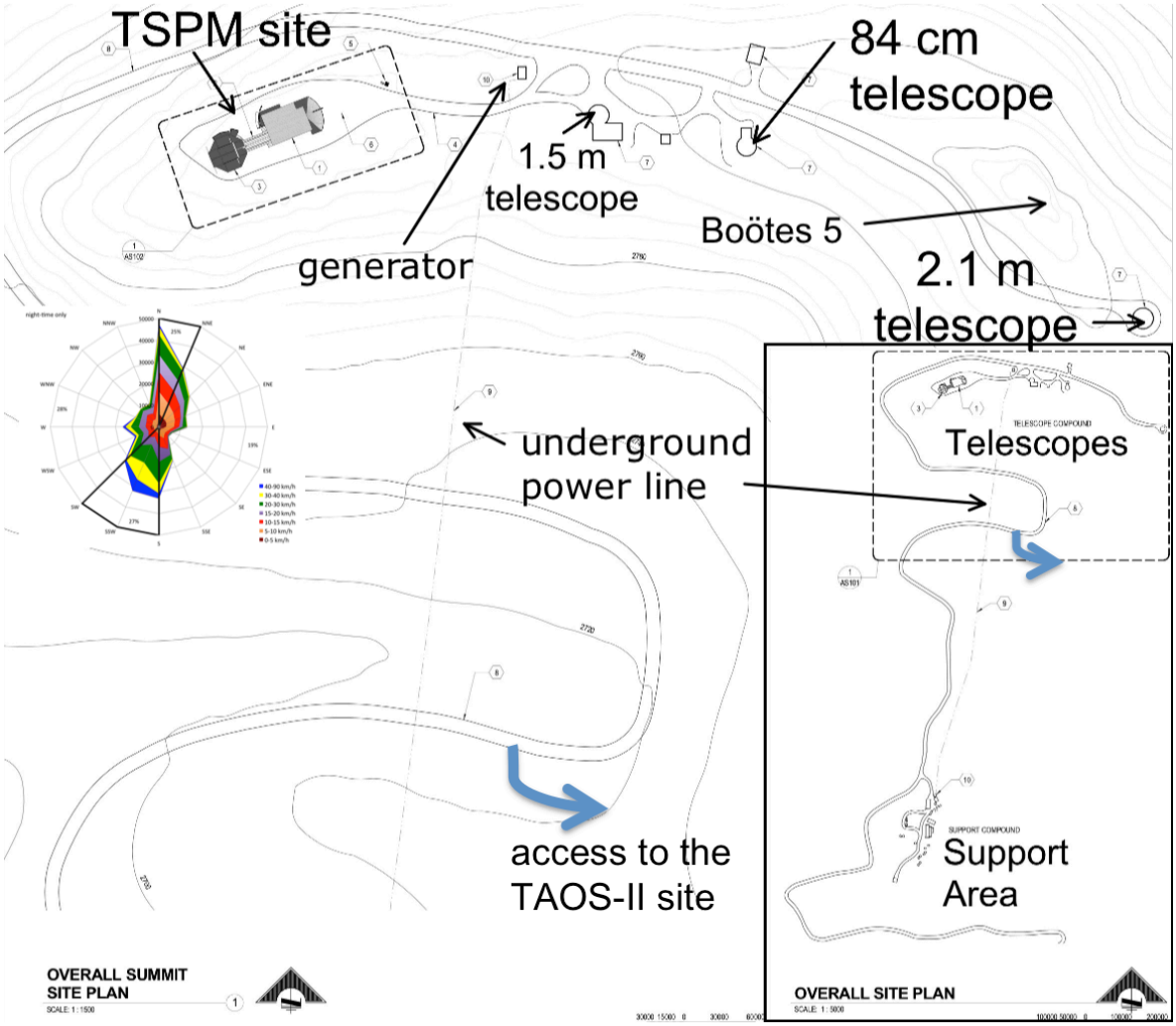

Figure 2: The main map shows the telescope area at the OAN-SPM in detail while the inset shows the overall layout of the facilities at the OAN-SPM. The TAOS-II project is located in an area to the east of the map, approximately 600 m east of the 2.1m telescope whose access is shown schematically. The

support area is about 2.5 km from the 2.1m telescope by road. There is a difference in elevation of about 200m between the two areas. Above centre at left, a wind rose for the wind at night is superposed.

The most obvious infrastructure at the OAN-SPM are the telescopes. For many years, there were three telescopes in operation. Recently, several new projects have begun and are in various stages of development:

- 1.5m: began operations in 1970
- 84cm: began operations in 1971
- 2.1m: began operations in 1979
- TAOS-II (3 1.3m telescopes): began construction in 2012, in collaboration with the Academia Sinica Instituto of Astronomy and Astrophysics (Taiwan) and the Smithsonian Astrophysical Observatory (USA)
- Boötes-5 (50 cm telescope): currently in commissioning, in collaboration with the Consejo Superior de la Investigación Científica (Spain) and Sungkyunkwan University (South Korea)
- COATLI (50 cm telescope): currently under construction
- DDOTI (60 square degree imaging system): currently under construction

Although the telescopes may be the most obvious infrastructure, they are really at the end of a chain of infrastructure that allows the OAN-SPM to be a viable observatory. Given the remoteness of the OAN-SPM, its viability depends upon maintaining the welfare of its personnel, both astronomers and support staff. The most fundamental elements of this support infrastructure are housing, energy generation, and transportation and communication services. Figure 3 shows the layout of this infrastructure in the support area at the OAN-SPM.

All personnel live in the main dormitory during their stay at the OAN-SPM. This building also includes the kitchen, dining hall, laundry services, an exercise area, television rooms, and some office space. There are separate sleeping areas for the personnel that work during the day and night. Formerly, the personnel lived in the "bungalows" (Figure 3), but these are now used only occasionally when the OAN-SPM hosts large groups, typically the result of official events. There is additional sleeping space with its own kitchen above the precision machine shop that is used mainly by contractors.

At present, the OAN-SPM is not connected to the national electricity grid. Work is underway to provide a connection to the national grid, which will probably occur in 2018. Thus far, all of the energy used at the OAN-SPM has been generated in situ with diesel generators. The main generators are in the support area. There are three main generators (Figure 4). They are used in rotation for periods of two weeks. From the generators, energy is supplied to the rest of the support area at low voltage, but is supplied to the telescope area via an underground power line at high voltage (13.5 kV). There is an "emergency" generator in the telescope area (Figure 2) that comes online automatically if the main power is lost (within 30 seconds). This generator can also supply power to the support area, but it is usually configured to supply only the telescope area. There is a

bank of fuel tanks near the main diesel generators and a smaller tank for the generator in the telescope area (for a total capacity of about 60,000 liters).

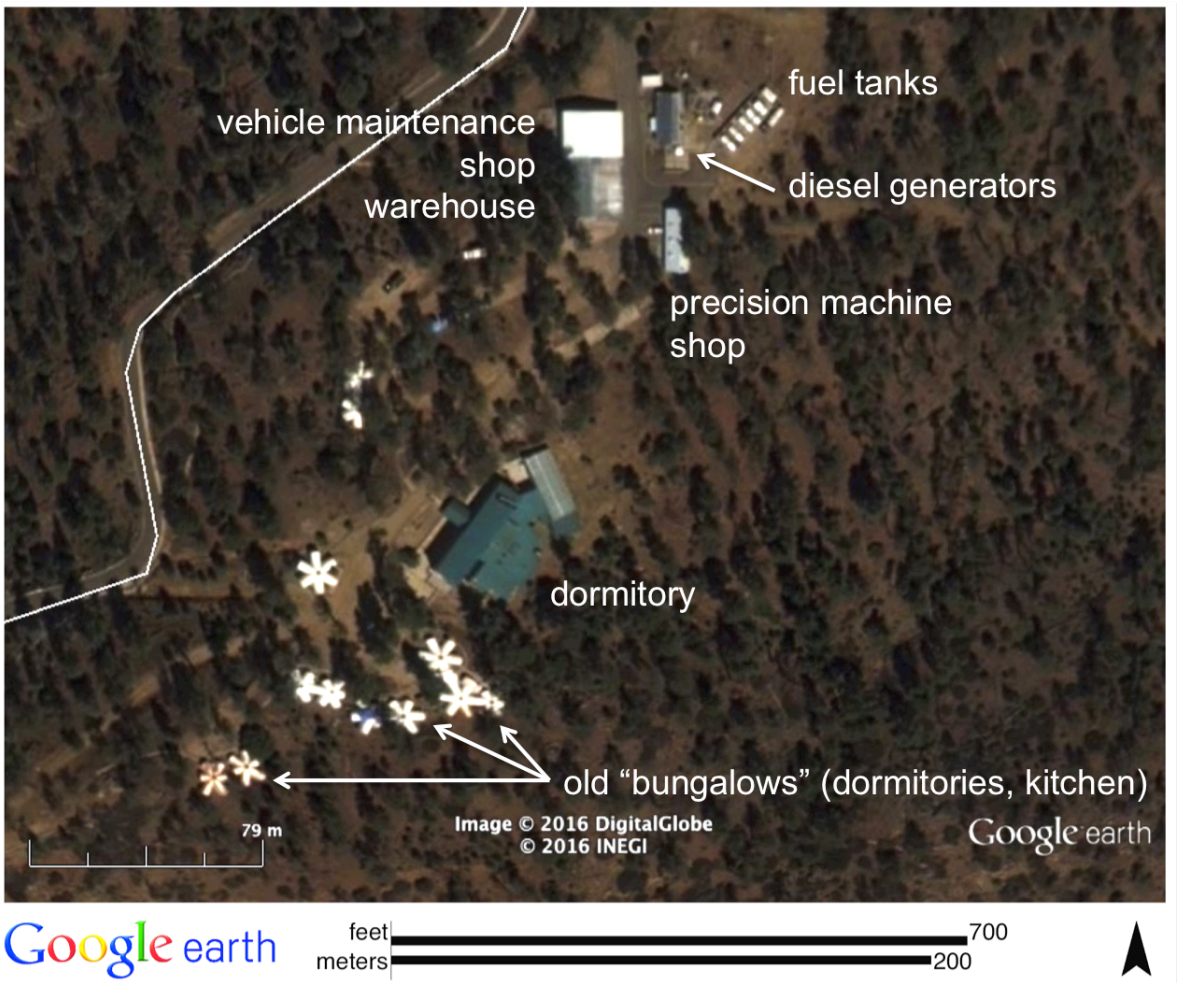

Figure 3: This Google Earth image shows the layout of the main area of the support compound in more detail. At the top are the warehouse, diesel generators, fuel tanks, and the machine shops for vehicle maintenance and precision machining. At bottom is the dormitory and the bungalows, which formerly were the dormitories and are now used only sparingly, mostly for surplus visitors during official events.

Once the OAN-SPM is connected to the national electricity grid, it is likely that one or two of the main generators will be taken out of service. Also, most of the fuel tanks will be decommissioned, since possible fuel leaks represent an environmental hazard.

The support area also contains a shop to maintain the OAN-SPM's fleet of vehicles as well as the machinery used for snow removal (Figure 3 and Figure 4). The two mechanics on duty are also charged with operating the diesel generators. In winter, the last approximately 30 km of the road leading to the OAN-SPM requires clearing after snowfalls.

Figure 4: These photos show various areas and activities within the support compound. At top left is the snow removal equipment used to maintain access to the OAN-SPM during the winter. At top right is the dormitory that houses astronomers and support staff at the OAN-SPM. At bottom left is the generator building. At bottom right, several of the staff practice putting out fires before the fire extinguishers are sent to be refilled.

Figure 5 presents two views of the telescope area. This area is a narrow ridge, about 90 m wide, that runs east-west and is about 200 m higher than the support area. The site chosen for the TSPM project is at the western end of this ridge. All of the current telescopes and ongoing telescope projects are on this ridge, except the TAOS-II project. The TAOS-II project is located on a hill to the east of the ridge shown in Figure 2 and Figure 5. Access to this area is shown schematically in Figure 2.

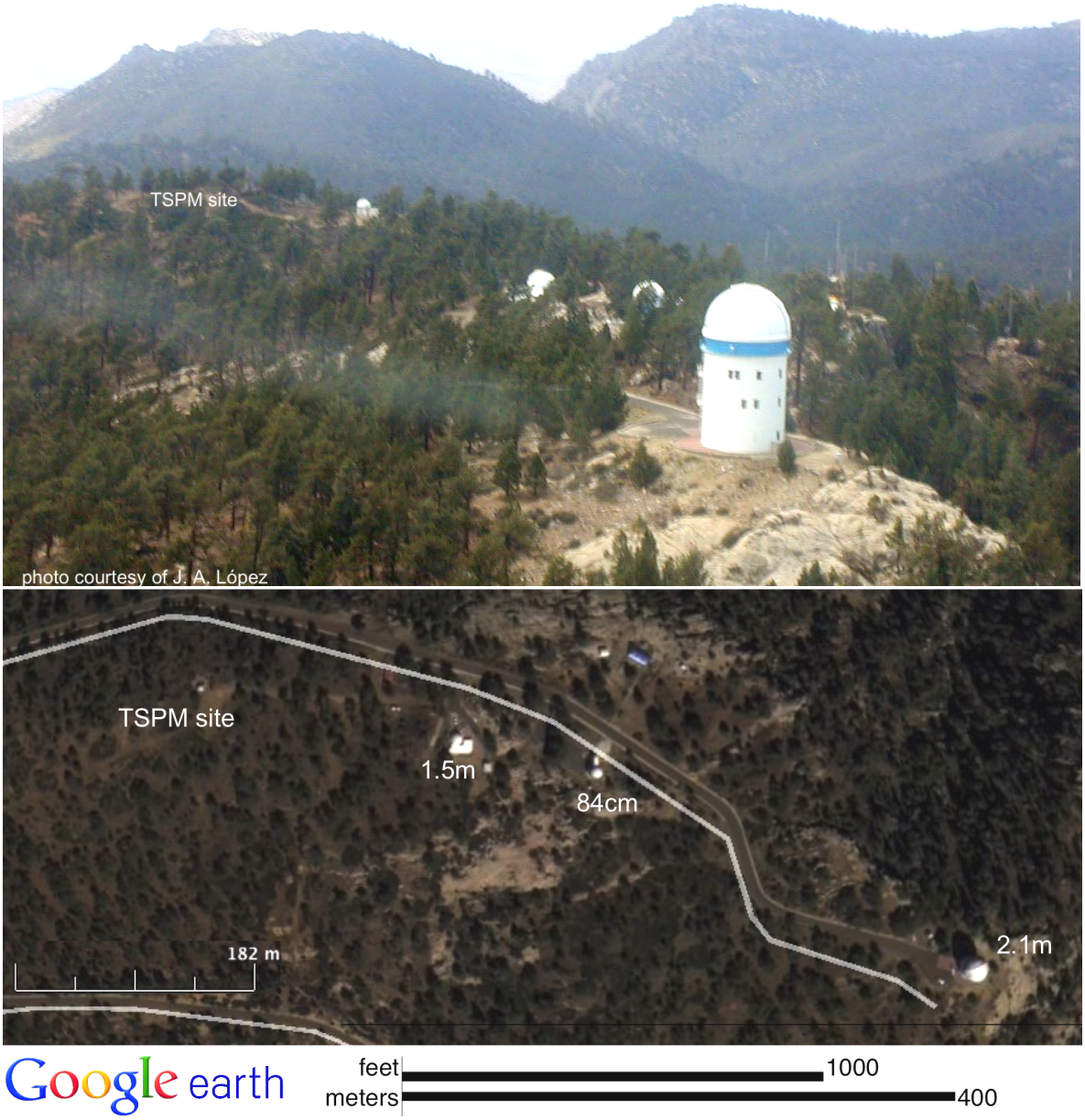

Figure 5: The two panels present aerial and "Google Earth" views of the telescope area at the OAN-SPM. The view in the top panel is from the east towards the west. From this panel, it is clear makes clear that the telescopes are located on a narrow ridge, about 90m wide, that runs nearly east-west. There is currently a small abandoned telescope dome near the TSPM site, which is at the western end of the ridge.

6. CLIMATE

During its 45-year history, there have been many studies of different aspects of the climate at the OAN-SPM. The first of these is probably that of Mendoza (1971), which covers primarily topics of

"astroclimate", i.e., sky brightness, precipitable water vapour, seeing, cloud cover, etc. (see §7). Alvarez & Maisterrena (1977) are the first to devote themselves to the weather at the OAN-SPM. Other notable published contributions are Tapia (1992), Echevarría et al. (1998), Michel et al. (2001, 2003), Tapia (2003), Tapia et al. (2007), Alvarez et al. (2007), and Bohigas & Núñez (2010). What follows concerning temperature and wind is based primarily upon data acquired with the LSST, TMT, and OAN-SPM facility weather stations over a nearly 9-year period from 02 Oct 2004 to 22 August 2013. The focus on these data sets should not be interpreted as indicating that these data are necessarily better than those mentioned above, as some of those studies use the same data, but rather that they represent the longest continuous data set available at the most recent epoch. Hence, they may better reflect current conditions at the OAN-SPM.

6.1 Temperature

A more extensive discussion of the material presented here may be found in reference document R.2. It is based upon data obtained with the OAN-SPM's weather station during the period 24 June 2006 to 22 August 2013. The meteorological station is a Davis Vantage Pro2 Plus model. The meteorological station was located on a 6m mast that was erected upon a rock outcrop about 3m high between the 1.5m and 84cm telescopes (see Figure 2).

Table 1 presents some overall statistics concerning the temperature at the OAN-SPM. There are sections for the entire period from Oct. 2004 to Aug. 2013 and for the four full years from 2009 to 2012, since, the weather station was not logged during the OAN-SPM's end of year closures prior to 2009. Table 1 indicates that the temperatures range from approximately -17 C to +24 C during the period under study, with median temperatures of 10.4 C during the day and 6.8 C at night during 2009-2012.

Table 1: Temperature Statistics

	Entire period			1 Jan 2009 to 31 Dec 2012		
Statistic	all data	day	night	all data	day	night
records	712541	365427	347142	415479	212138	203342
mean temperature	8.3	9.8	6.6	8.0	9.6	6.4
median temperature	9.0	10.8	7.2	8.6	10.4	6.8
minimum temperature	-16.7	-15.0	-16.7	-16.7	-15.0	-16.7
maximum temperature	23.9	23.9	21.8	23.3	23.3	19.1

Note: All temperatures are given in degrees Celsius.

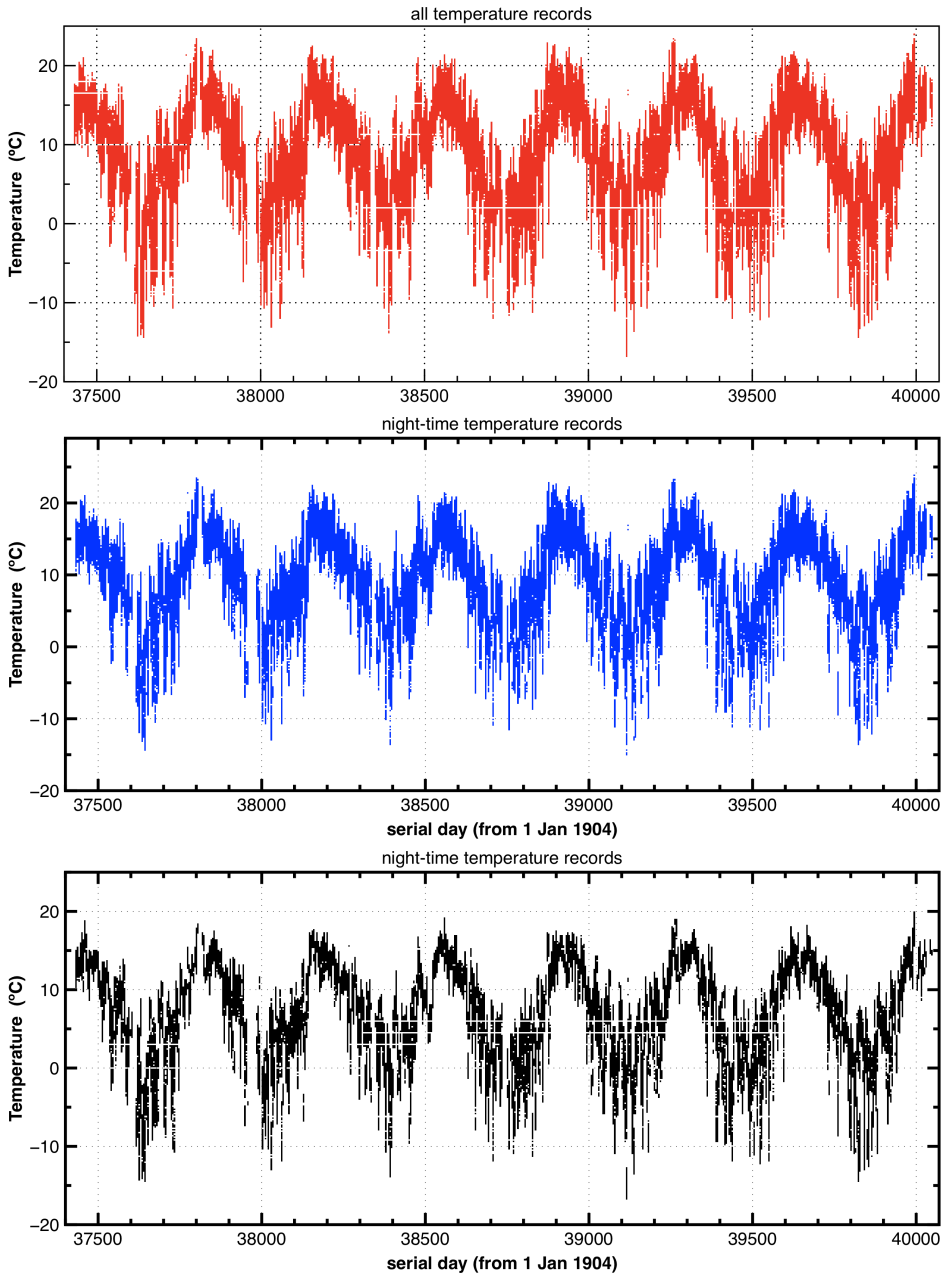

Figure 6: The three panels present all of the temperature records as a function of time for the OAN-SPM's weather station. The top panel presents all of the data while the middle and bottom panels present the data acquired during daytime and night-time, respectively. There is more variation in temperature during winter (colder temperatures) and during the day (most noticeable during summer). For reference, the civic date corresponding to serial day 37500 is 1 September 2006 UT.

In Figure 6, all of the temperature records from the OAN-SPM's weather station are plotted as a function of time. This is done for all records (top panel), records during the day (middle), and

records during the night (bottom). It is immediately clear that the temperature variation is greater in winter (when the lowest temperatures occur) than in summer. Although it is not so evident, there is also greater temperature variation during the day than at night, which is most easily seen by comparing the scatter during the summer for the panels with day-time and night-time records.

From Figure 6, it is clear that there is a strong seasonal temperature variation. Figure 7 presents the seasonal variation in more detail, dividing the data by month and plotting the mean temperature as a function of the month of the year. February is the coldest month while July and August are the warmest, with mean night-time temperatures that vary from 0 C to 14 C. Figure 7 also shows that the variation in mean temperature between night and day varies little during the year, falling within the range of 1.8-2.2 C, except during March-June, when it can reach values up to 3 C.

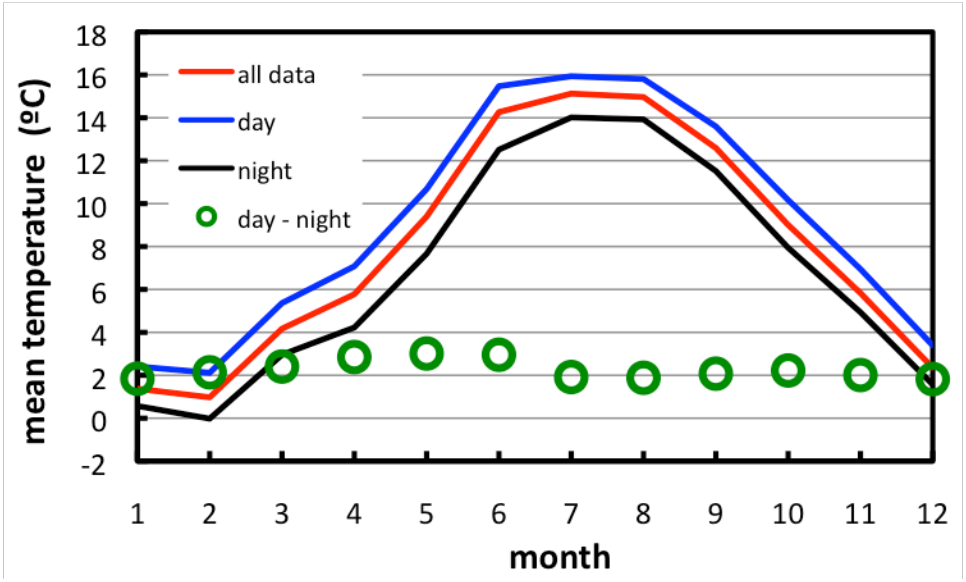

Figure 7: The mean temperature at the OAN-SPM shows a pronounced variation through the year. Even so, the difference between the monthly daytime and night-time average temperatures (circles) is relatively constant at 1.8-2.2 ºC, only in March-June does it stray outside this range, reaching approximately 3 ºC in May-June. For reference month 1 is January and 12 is December. The data span the period from Oct. 2004 to Aug. 2013.

In Figure 8 the data are plotted as a function of time throughout the day, normalized by some fiducial value. In the left column, this fiducial value is the mean temperature that day. On the right, it is the temperature at sunrise. Clearly, there is much less temperature variation during the night than during the day. It is also evident that sunrise is the coolest moment, on average, each day.

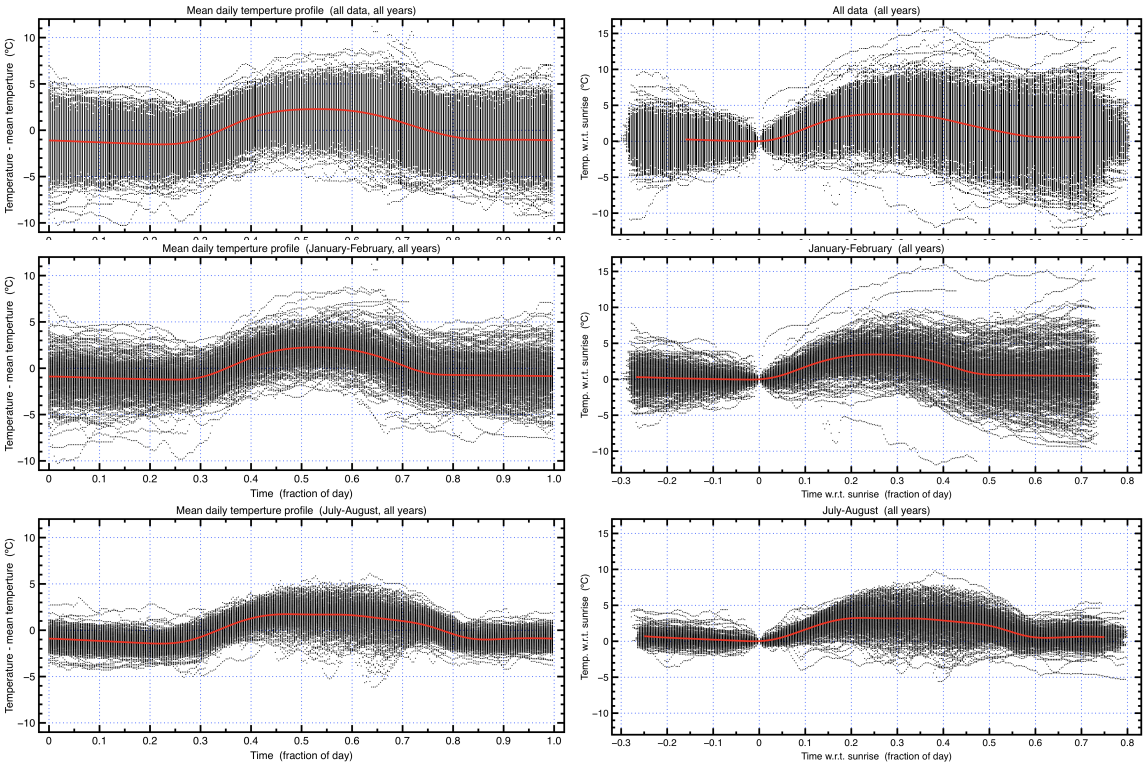

Figure 8: In both columns, the three panels present the temperature each day as a function of time during the day, midnight being at 0.0, with respect to the average temperature that day (left) and the temperature at sunrise (right). The top row amalgamates all of the data in the entire dataset (June 2006 to Aug. 2013) while the middle and bottom rows present the data from January-February and July-August, respectively (for the years 2007-2013 in both cases). Comparing the middle and bottom rows clearly shows that there is greater temperature variability in winter than in summer and during the day than at night. There is a very gradual cooling from sunset to sunrise, with sunrise being the coolest moment of the day.

Figure 9 presents the distribution of the temperature excursion during daytime, at night, and over a full day. Table 2 presents related statistics. From Figure 9, it is clear that there is greater temperature variation during the day than at night. The temperature excursion during the day is nearly constant at 5-6 C for July to February, but somewhat greater March through June. At night, the temperature excursion is least from May to September, with a minimum value of about 2 C, and is in the range of 3-4 C the rest of the year. The median value of the temperature excursion over a full day is 5.9C (Table 2, Figure 9 bottom left), with a minimum variation during July to September and a maximum variation from April to June.

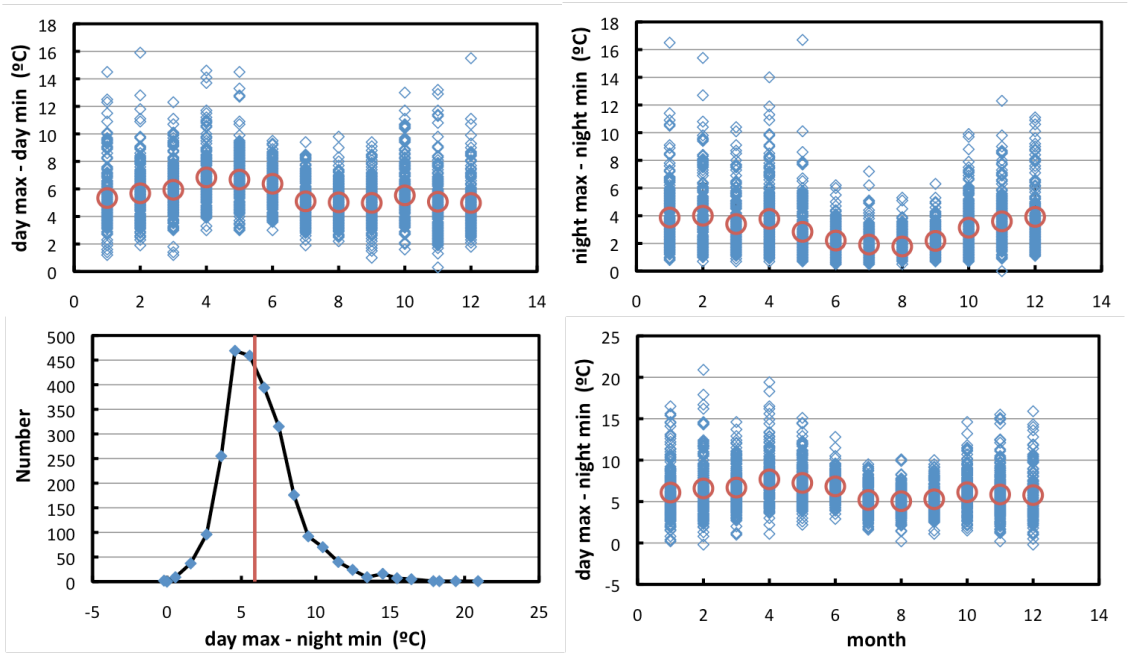

Figure 9: These panels present characteristics of the daily temperature excursion for each day (June 2006 to Aug. 2013). In the top row, the two panels present the temperature excursion during day- and night-time (left and right, respectively) during each month of the year. The red circles are the means of the individual values (blue diamonds). The greater temperature excursion during daytime is clear. The bottom row considers the total daily temperature excursion, from daytime high to night-time low. The vertical line in the left panel indicates the median value (Table 2). The circles in the right panel indicate the mean value for each month. The total daily temperature excursion is highest during April-June and lowest in July-September.

Table 2: Day, Night, and Day-Night Statistics

Parameter	Statistic maximum	minimum	median	mean
day mean – night mean	10.1	-10.6	2.3	2.2
day max. – day min.	15.9	0.3	5.5	5.6
night max. – night min.	16.7	0.0	2.5	3.0
day max. – night min.	20.9	-0.2	5.9	6.2

Figure 10 presents the correlation between the temperature at sunrise and at sunset later the same day. Clearly, the correlation is very good. For sunrise temperatures exceeding 0 C, the difference between sunset and sunrise temperatures the same day is 1 C or less with a dispersion of ±2 C.

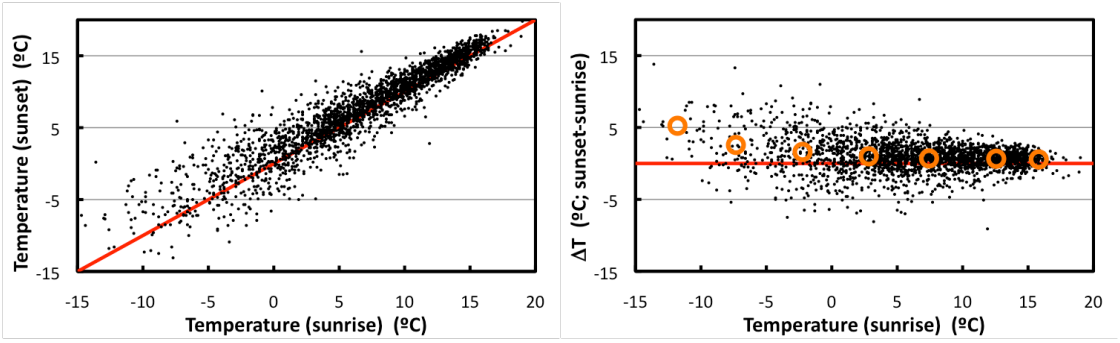

Figure 10: This figure illustrates the correlation between the temperatures at sunrise and sunset on the same day (Oct. 2004 to Aug. 2013). The left panel plots the sunset temperature as a function of the sunrise temperature earlier that same day. The right panel plots the difference between sunset and sunrise temperatures on a given day as a function of the sunrise temperature that day. In both panels, the red line indicates equality of the sunrise and sunset temperatures. The orange circles in the right panel represent the average temperature difference for 5 ºC temperature bins (Table 6). It is evident from both panels that the sunset temperature differs more from the sunrise temperature as the latter gets cooler. At cooler sunrise temperatures, the scatter is greater. For temperatures exceeding 0 C (which occur 85% of the time), the mean difference between sunset and sunrise temperatures is less than 1 C with a scatter of approximately ±2 C.

The distribution of hourly temperature gradients is shown in Figure 11 considering all data as well as data taken during the day and at night. The gradients are defined as the temperature at a given moment minus the temperature an hour later. Thus, negative values occur when the temperature is increasing and positive ones when the temperature is decreasing. The distributions of hourly temperature gradients are very different during the day and night, reflecting the temperature variations outlined above. At night, the distribution of hourly temperature gradients is very narrow, with 84.6% of all values less than an absolute value of 0.6 C/hour and only 4.9% exceeding an absolute value of 1.0 C/hour. During the day, only 50% of the hourly temperature gradients are below an absolute value of 0.6 C/hour and 25% exceed an absolute value of 1.0 C/hour. Not surprisingly, the largest gradients during the day occur in the hours immediately after sunrise or before sunset.

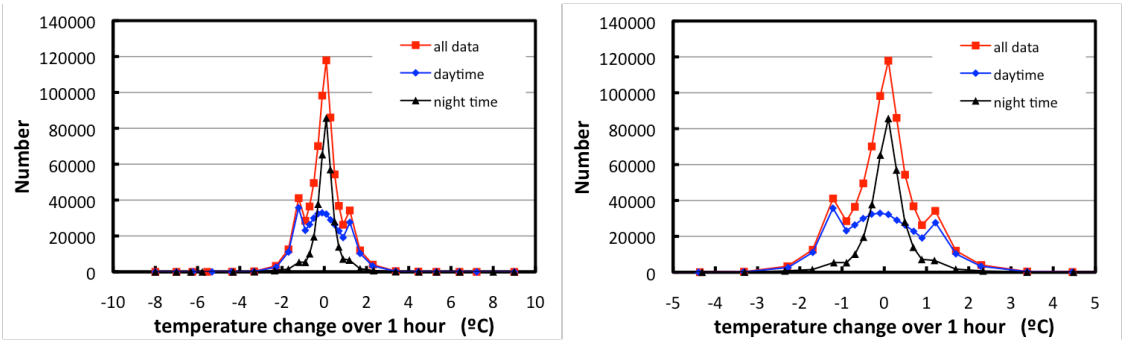

Figure 11: The distribution of hourly gradients is shown, displaying the full range of values and considering centre of the distribution. To compute this distribution, the temperature records were first smoothed using a boxcar function over ±30 minutes to produce a smoothed temperature record. The

hourly gradient is then the difference in (smoothed) temperature from a given time to the (smoothed) temperature 60 minutes later, so negative values occur when the temperature is increasing with time and positive values when it is decreasing (cooling). 99.9% of all records from the entire data set were used (Oct. 2004 to Aug. 2013). The distributions of the hourly gradients differ significantly between day and night, with night-time temperature gradients being generally smaller.

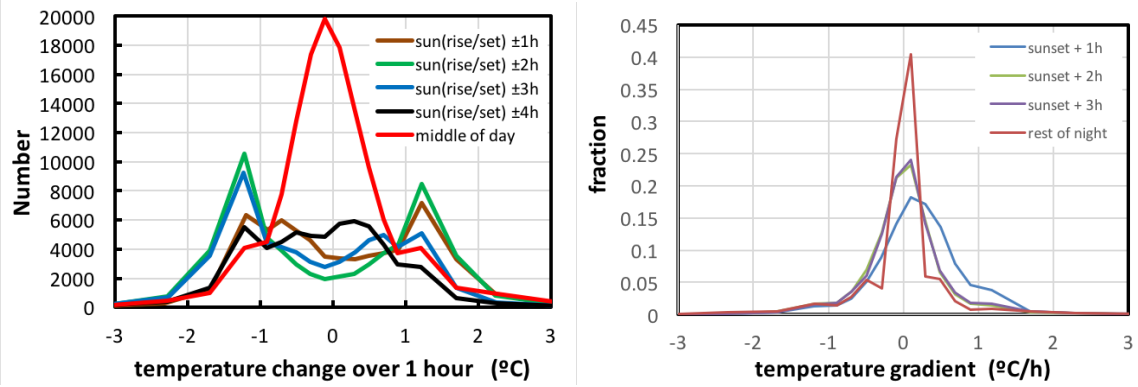

Figure 12: These figures present details of the evolution of the temperature during the day (left) and night (right). Clearly, the largest temperature gradients occur after sunrise and before sunset. The curve for "middle of day" represents all data more than 4 hours from sunrise or sunset, and is equivalent to approximately two hours of data, strongly weighted towards summer. At night (right), the cooling continues during the first hour after sunset (positive gradients), but thereafter the distribution of temperature gradients is similar to that during the rest of the night. Since there is much more data in the "rest of night" curve than the others, the fraction of data at each gradient is plotted to better distinguish differences. There is little difference between the distributions of temperature gradients during the second and third hours after sunset.

The left panel of Figure 12 presents details of the temperature evolution during the day. The temperature gradients show an excess of large values (negative values) in the hour immediately after sunrise, but this excess is strongest during the second and third hours after sunrise. By the fourth hour after sunrise, the excess has decreased. At sunset, the situation is somewhat different, since strong cooling (positive gradients) become noticeable during the third hour before sunset, but is strongest in the two hours immediately preceeding sunset.

The right panel of Figure 12 presents details of the temperature evolution after sunset. During the first hour after sunset, the temperature gradients present an excess of large values, indicating that the strong cooling that occurs just prior to sunset continues. Note, however, that the absolute value of the temperature gradients after sunset are considerably smaller than those before sunset. The distribution of temperature gradients during the second and third hours after sunset are very similar and are a much better approximation to the distribution of gradients during the rest of the night, as expected from Figure 8.

Table 3 presents percentiles for the distributions of a variety of temperature-related parameters. The full distributions may be found in reference document R.2.

Table 3: Percentile values for the distributions of temperatures and hourly temperature gradients

		Percentiles					
Distribution		5%	10%	25%	75%	90%	95%
all temperatures	(ºC)	-4.0	-1.0	3.9	13.4	15.9	17.3
daytime temperatures	(ºC)	-2.5	0.7	5.6	14.7	17.2	18.5
daytime average	(ºC)	-2.5	0.6	5.4	14.4	16.9	17.8
daytime median	(ºC)	-2.1	0.8	5.7	14.6	17.2	18.3
daytime maximum	(ºC)	0.1	3.1	7.8	16.8	19.3	20.5
daytime minimum	(ºC)	-12.3	-3.2	2.1	11.7	13.9	14.8
night-time temperatures	(ºC)	-5.3	-2.2	2.5	11.8	14.3	15.3
night-time average	(ºC)	-4.7	-1.6	3.0	12.3	14.5	15.4
night-time median	(ºC)	-4.6	-1.5	3.2	12.5	14.6	15.5
night-time maximum	(ºC)	-2.1	0.5	4.7	13.5	15.4	16.4
night-time minimum	(ºC)	-7.3	-3.8	1.2	11.3	13.7	14.7
day mean – night mean	(ºC)	-0.9	0.0	1.1	3.3	4.6	5.3
day max. – day min.	(ºC)	3.0	3.5	4.3	6.7	8.0	8.9
night max. – night min.	(ºC)	0.9	1.2	1.6	3.7	5.5	7.0
day max. – night min.	(ºC)	2.8	3.5	4.5	7.4	9.2	10.7
hourly gradients all data	(ºC/hour)	-1.21	-0.90	-0.38	0.37	0.84	1.17
hourly gradients day	(ºC/hour)	-1.41	-1.14	-0.66	0.54	1.07	1.40
hourly gradients night	(ºC/hour)	-1.64	-0.47	-0.18	0.29	0.56	0.78
sunrise temperature	(ºC)	-4.9	-2.1	2.8	12.2	14.3	15.0
sunset temperature	(ºC)	-4.1	-0.9	3.7	12.8	15.0	16.0
sunset – sunrise temp diff	(ºC)	-2.4	-1.3	-0.1	2.0	3.4	4.7

Note: All temperatures are given in degrees Celsius and hourly temperature gradients are given in degrees Celsius per hour.

Alvarez & Maisterrena (1977) also report an annual temperature variation similar to that reported here, though they find that March is the coldest month and July the warmest. The temperature range between these months, of 18 C, is slightly greater than we find here, 15 C. On the other hand, Bohigas & Núñez (2010) find that January is the coldest month and July the warmest. They also find similar values to those reported here for the temperature excursion during the night and over an entire day (maximum to minimum). Clearly, the precise sampling interval and location of the weather station have some effect upon the results. As found here, Michel et al. (2003) report that there is greater dispersion in the ambient temperatures in winter and during the day.

6.2 Wind

A more extensive discussion of the material presented in this section may be found in reference document R.1 and R.15. It is based upon data obtained with four different anemometers during the period 02 Oct 2004 to 22 August 2013, three of which were close to or at the site chosen for the TSPM project. The fourth was attached to the OAN-SPM's meteorological station that was located

on a 6m mast that was erected upon a rock outcrop about 3m high between the 1.5m and 84cm telescopes (see Figure 2).

The data analysis concerns three primary issues: wind velocities, wind directions, and the vertical structure of the temperature and wind velocity. For wind velocities, no distinction is made between data obtained during daytime and at night. For the wind directions, we distinguish between the two cases, though here we only present the data obtained at night. For the vertical structure of the wind, data are only available for night-time.

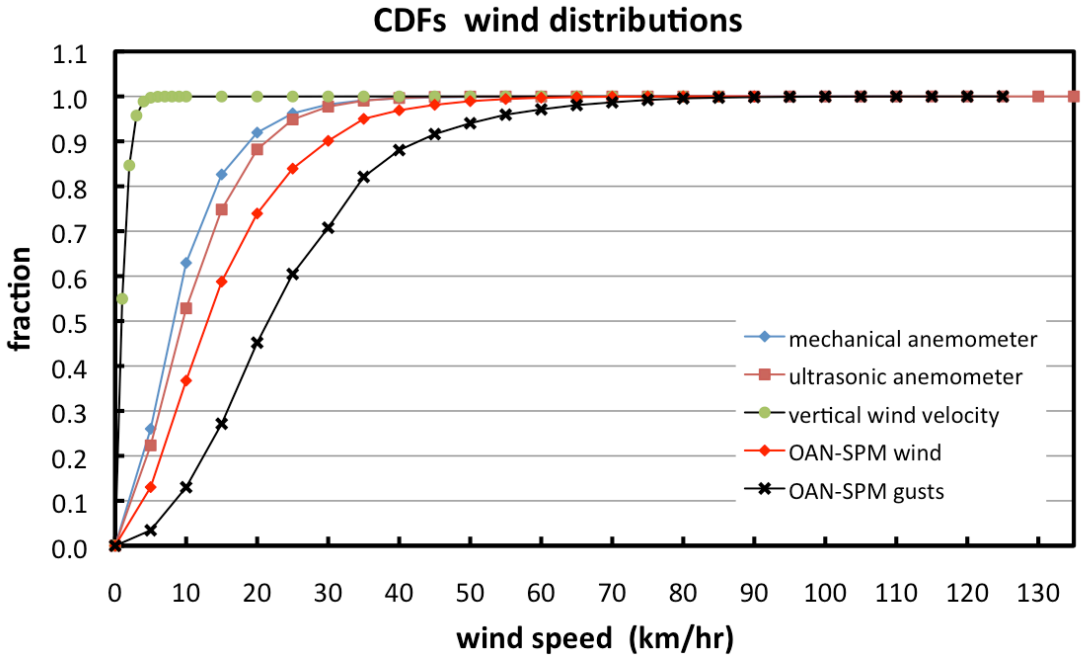

Figure 13: This figure presents the cumulative distributions for the wind speeds measured with three anemometers (Table 4 and Figure 14 presents wind roses based upon data acquired at night using the mechanical anemometers attached to the OAN-SPM (left) and TMT (right) weather stations. Generally, they are similar, indicating that the most common wind direction is from the S to SSW, but followed very closely in frequency by winds from the opposite direction, N to NNE. Likewise, both indicate that winds stronger than 20 km/h are more common from the S to SSW than from other directions. Winds from either the E or W are much less common.

Table 5). The "mechanical" and "ultrasonic" anemometers were attached to the LSST's weather station and represent the average wind speed in one-minute intervals. The vertical wind velocity was measured with the LSST's ultrasonic anemometer and is the average wind speed in one-minute intervals. The OAN-SPM "wind" and "gusts" were measured with the OAN-SPM's mechanical anemometer. The "wind" measurements represent the average wind speeds measured in five-minute intervals while the "gusts" are the maximum readings in each of those five-minute intervals.

Starting with the distribution of wind velocities, Figure 13 presents cumulative distributions of the wind velocities recorded by the different anemometers. In general, the distributions are in qualitative agreement with the results indicated above, since the order of height among the anemometers included is "mechanical anemometer", "ultrasonic anemometer", and "OAN-SPM wind" at heights of 2m, 7m, and 9m, respectively. The results of the wind rose for the ultrasonic anemometer (see reference document R.1) indicate that its wind speed distribution is likely skewed to lower values, so not too much should be read into its similarity to the LSST's mechanical anemometer. Since the OAN-SPM's mechanical anemometer is closest in height to the TSPM, its results are perhaps the most relevant.

Table 4: The distribution of wind speeds measured by the LSST's weather station.

Speed	mechanical anemometer		ultrasonic anemometer	
(km/h)	count	CDF	count	CDF
5	181292	0.260	94609	0.223
10	257412	0.630	129193	0.528
15	137180	0.826	93165	0.748
20	64907	0.919	56685	0.882
25	29811	0.962	28261	0.949
30	13855	0.982	12085	0.977
35	6490	0.991	5641	0.991
40	2982	0.996	2481	0.996
45	1468	0.998	1012	0.999
50	751	0.999	339	0.9996
55	377	0.9995	60	0.99976
60	168	0.9997	2	0.99977
65	103	0.9998	2	0.99977
70	53	0.9999	1	0.99977
75	25	0.99996	1	0.99978
80	14	0.99998	7	0.99979
85	7	0.99999	11	0.99982
90	3	0.999993	3	0.99983
95	1	0.999994	3	0.99983
100	2	0.999997	10	0.99986
105	1	0.9999999	28	0.99992
110	1	1.0	12	0.99995
115			10	0.99997
120			5	0.99999
125			2	0.99999
130			2	0.999995
135			2	1.0
records	696903		423632	

Note: The "count" for a given speed indicates the number of measurements between that speed and the next lowest speed, i.e., there were 181292 measurements with speeds between 0 and 5 km/h.

Based upon the data presented in Table 5, the sustained wind speed (five-minute average) is less than 50 km/h 98% of the time. For the same fraction of time, wind gusts are less than 65 km/h and the difference between the gusts and sustained wind speed is less than 25 km/h.

Figure 14 presents wind roses based upon data acquired at night using the mechanical anemometers attached to the OAN-SPM (left) and TMT (right) weather stations. Generally, they are similar, indicating that the most common wind direction is from the S to SSW, but followed very closely in frequency by winds from the opposite direction, N to NNE. Likewise, both indicate that winds stronger than 20 km/h are more common from the S to SSW than from other directions. Winds from either the E or W are much less common.

Table 5: The distribution of wind speeds, gusts, and their difference from the OAN-SPM's mechanical anemometer.

Speed	winds		gusts		gust-wind	
(km/h)	count	CDF	count	CDF	count	CDF
5	81839	0.130	22270	0.034	173507	0.269
10	148704	0.367	61886	0.130	245742	0.650
15	138181	0.588	91352	0.271	135353	0.859
20	95121	0.739	116660	0.452	58421	0.950
25	62716	0.839	98767	0.605	22009	0.984
30	38765	0.901	66632	0.708	7336	0.995
35	30714	0.950	73091	0.821	2229	0.999
40	11992	0.969	38555	0.881	612	0.9996
45	7584	0.981	22995	0.916	188	0.9999
50	5126	0.989	15662	0.940	49	0.99996
55	2992	0.994	12291	0.959	13	0.99998
60	1786	0.997	7633	0.971	9	0.999989
65	882	0.998	6173	0.981	2	0.999992
70	585	0.999	3971	0.987	5	1.0
75	271	0.9998	3486	0.992		
80	72	0.9999	2173	0.996		
85	31	0.99999	1117	0.997		
90	4	1.0	715	0.998		
95			445	0.999		
100			279	0.9995		
105			175	0.9998		
110			62	0.9999		
115			31	0.99996		
120			17	0.99998		
125			10	1.0		
records	627346		646449		645475	

Note: The sustained winds are 5 min. averages and the gusts are the max. wind speed during the 5 min. interval. The difference is computed in each 5 min. interval. The "count" is calculated as in Table 4.

Figure 15 indicates, however, that the distribution of wind directions varies seasonally. Winds from the N to NNW dominate from July to November, but are much less common from December to

June. For this analysis, we only use the data from the OAN-SPM's mechanical anemometer since its data are more complete (see reference document R.1).

The most detailed study with which to compare the foregoing is that of Bohigas & Núñez (2010), based upon data acquired with the mechanical anemometer from the LSST/TMT weather station. Very generally, their results are in good qualitative agreement with those presented above: They find that winds from the N to NE dominate in summer and fall, that there is a slight dominance of winds from S to SW at night, followed by those from N to NE (and the reverse during the day). One issue that they study that is not reported above is that the wind speed distribution is shifted to higher speeds at night, with wind speeds at night being approximately 25% greater than those recorded during daytime.

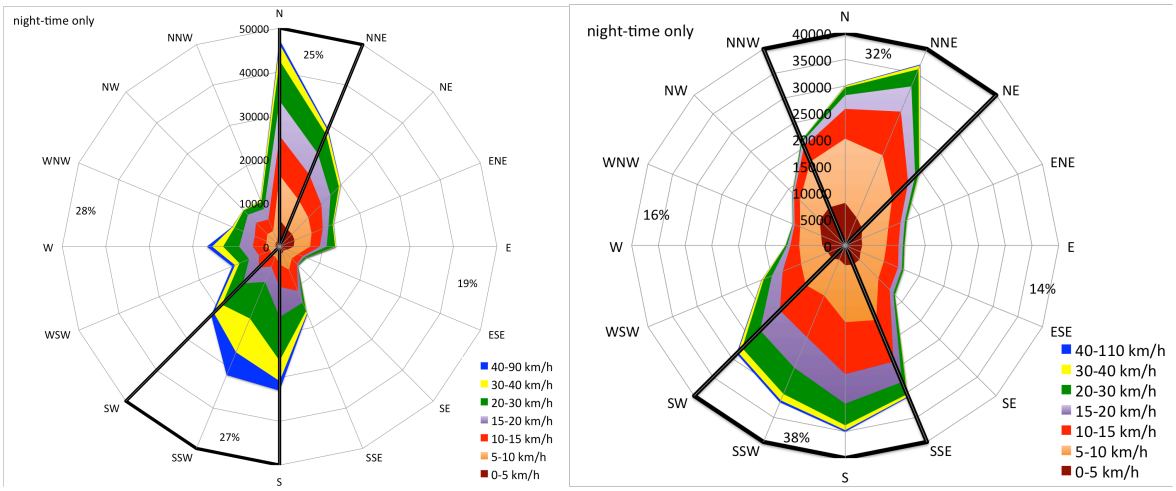

Figure 14: These wind roses are derived from measurements with the mechanical anemometers belonging to the OAN-SPM's weather station (left) and the TMT's weather station (right) for measurements made at night only. The black lines enclose the dominant directions from which the wind blows. The percentages indicate the fraction of records in each sector, i.e., for the OAN-SPM's mechanical anemometer, 27% of the records are for winds with directions S, SSW, and SW. There is very broad agreement between the measurements from the two anemometers. The most common direction for winds at night is from the S to SSW, but this is followed very closely by winds from the N to NNE. The contribution from the strongest winds, exceeding 20 km/h, is greater from the south (and west) than from the north (or east).

Alvarez & Maisterrena (1977), Echevarría et al. (1998), and Michel et al. (2001, 2003) also studied the winds at the OAN-SPM. Alvarez & Maisterrena (1977) also find that the winds are systematically stronger at night than during the day. Echevarría et al. (1998) find a much more uniform wind distribution that found here or reported by Bohigas & Núñez (2010). The studies of Michel et al. (2001, 2003) use the same equipment, but cover different time intervals. While Michel et al. (2001) find a distribution of wind directions similar to what we report and reported by Bohigas & Núñez (2010), Michel et al. (2003) find a distribution more like that reported by Echevarría et al. (1998). Michel et al. (2003) also report that the wind speed distribution at night is

shifted to higher speeds than during the day and that, at night, winds from the S to SW are more common than winds from the N to NE, but that the reverse is true during the day.

As a final comment on the wind speeds, we point out that the typical wind speeds at the OAN-SPM are lower than at many observatories (Schöck et al. 2009).

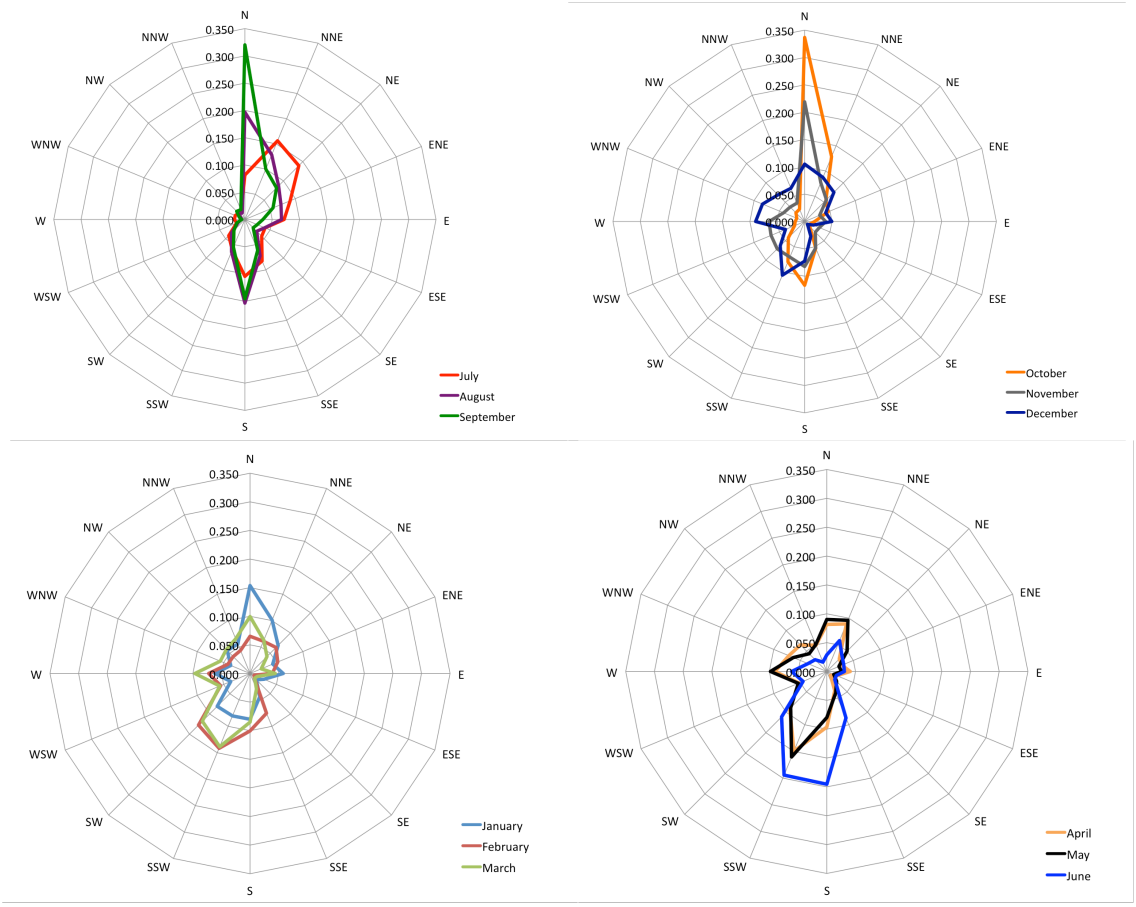

Figure 15: The wind roses for the OAN-SPM's mechanical anemometer for different months of the year vary significantly. Here, only night-time data is included. To account for the variable number of records for each month, the wind roses are plotted using the fraction of records for each month from each direction. Winds from the N dominate strongly from July to November, but are much less frequent from December to June.

Concerning the vertical structure of the wind at the OAN-SPM, Bohigas & Núñez (2010; Figure 16), were the first to analyze this and used data from the ultrasonic anemometers that were installed on a 30 m tower for approximately six months by the LSST/TMT site testing group. They find that the wind speed increases in proportion to the logarithm of the height above the ground, as shown in the left panel of Figure 16. Subsequently, R.15 studied this issue, using one minute time intervals, rather than whole nights as in Bohigas & Núñez (2010), with very similar results (top right panel;

Figure 16). The wind speed increase with height has some structure depending upon the wind direction, with the increase being greatest for winds blowing from the north and west (bottom right panel; Figure 16).

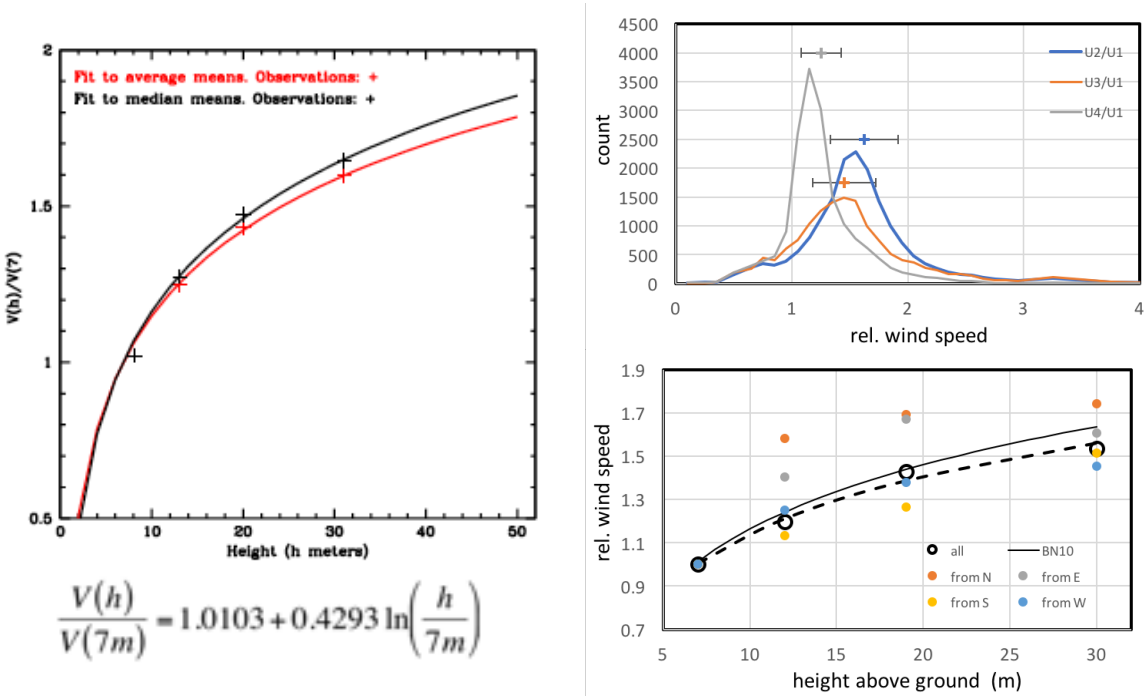

Figure 16: All of these figures are based upon data acquired by the LSST project using a mast 30 m tall with sonic anemometers at heights of 7 m, 12 m, 19 m, and 30 m. On the left, is the median velocity as a function of height found by Bohigas & Núñez (2010), which is based upon data averaged over entire nights. At top right, we show the distributions of 60 second averages (R.2) of the wind speed measured at 12 m (U4), 19 m (U3), and 30 m (U2) relative to that at 7 m (U1). The crosses in the top panel show the median values from Bohigas & Núñez (2010). At bottom right, we present the median wind speed as a function of height segregated according to the wind direction (Richer & Núñez 2017). The thin solid line is the relation from Bohigas & Núñez (2010; black, left column).

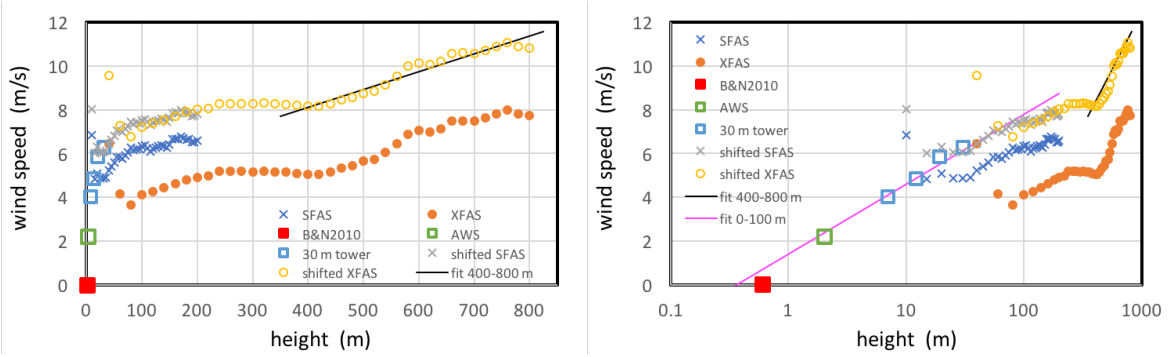

Figure 17: These figures present all of the data available concerning the vertical velocity profile of the wind for the TSPM site. The right panel differs from the left only in that the abscissa has a logarithmic scale. The raw SODAR data are shifted with respect to the measurements at lower heights, by +1.2 and

+3.1 m/s for the SFAS and XFAS instruments, respectively. Applying this shift, the velocity profile is continuous over the entire range of heights, from the roughness length (0.6 m; Bohigas & Núñez 2010) at which the air is stationary to a height of 800 m. The fit in the left panel (black line) includes all data between 400 and 800 m. The second fit in the right panel (magenta line) is to all of the data below 100 m, except the lowest SFAS data point.

The variation of the wind speed in proportion to the logarithm of the height found within the first 30 m of the ground in Figure 16 continues to heights of at least 100 m above the ground, as shown in the right panel of Figure 17. The additional data in Figure 17 was acquired by the TMT project using a variety of instruments to explore wind speeds up to heights of 800 m above the ground. In the height interval 100-200 m above the ground, the wind speed continues to rise, though more slowly than at lower heights (left panel; Figure 17). From approximately 200 m to 400 m, the wind speed remains nearly constant, but thereafter begins to increase again in a linear fashion to the limit of the data with a speed gradient equivalent to 8 (m/s)/km (left panel; Figure 17).

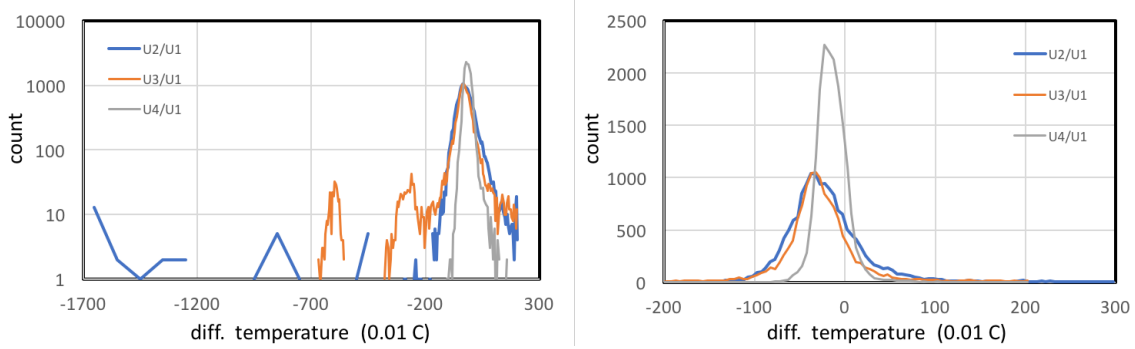

Figure 18: The two panels present the distributions of difference in temperature at 12 m (U4), 19 m (U3), and 30 m (U2) above the ground with respect to the temperature at a height of 7 m (U1). Note that the ordinate of the left plot is logarithmic in order to show the small number of measurements for temperature differences below -2 C. Note also that the bin size increases by a factor of 20 for temperature differences below -7 C. From this panel, it is clear that the main peaks of the distributions at heights of 19 m and 30 m are very similar. The right panel presents the main peak of the distributions on a linear scale. Again, the distribution of temperature differences at 19 m and 30 m is very similar, both in mean/median value and dispersion. In contrast, the distribution of temperature differences at 12 m differs, being shifted to lower values and presenting considerably less dispersion.

Figure 18 presents the variation of the temperature as a function of height above the ground for the first 30 m. These data were again acquired using the ultrasonic anemometers from the 30 m tower installed by the LSST project. The histograms in both panels of Figure 18 show the temperature measured at heights of 12 m, 19 m, and 30 m with respect to those measured at a height of 7 m above the ground. When progressing from a height of 7 m to 12 m, the temperature decreases by a median value of approximately 0.15 C. Going to heights of 19 m and 30 m, there is another similar decrease in the median temperature by a similar amount, for a total temperature change of about -0.3 C.

Finally, the only study of the wind power spectrum at the OAN-SPM is that of Hiriart, Ochoa, & García (2001, RMxAA, 37, 213). They made their measurements at the TSPM site with a sonic anemometer at a height of approximately 10m above the local terrain. Note that these measurements were made before trees were removed in 2005. Their main result is that the spectrum shape depends upon the direction from which the wind blows. Of their five time series, two arrive approximately from the east and the other three approximately from the south. Wind approaching from the south directly impacts the ridge occupied by the TSPM site (the same is true of wind from the west), while wind approaching from the east runs over the entire ridge upon which the telescopes are located (winds from the north are presumably an intermediate case). The spectra for the time series for winds from the south have a shallower slope and a higher maximum frequency, of order 0.015 Hz, while the spectra for winds from the east have steeper slopes and lower maximum frequencies, below 0.01 Hz. Therefore, as compared to winds that impact the ridge directly, it appears that winds from the east interact with the terrain, which presumably weakens the power available at higher frequencies.

6.3 Severe weather

Figure 19: This photo shows the dome for the 1.5m telescope as access was restored to the OAN-SPM after the severe winter storm in January 2010. Photo courtesy of Ignacio González.

Historically, severe weather only occurs in the form of winter snowstorms and summer thunderstorms. The latter occur every summer and the only defense is adequate grounding of all electrical installations and isolating sensitive equipment, such as instruments, to the extent that's practical, e.g., using optical fibre for communication lines through dome walls. Long lengths of substantial cable are particularly susceptible to induced charges that can damage or destroy connected equipment, including not only low voltage transmission lines, but also serial communication over RS-232.

As for severe winter storms (see Figure 19), they occur once to twice per decade. Historically, these storms have occurred in 1978, 1979, 1987, 1988, 1993, 1998 (twice), and 2010. The total is thus 8 events in 45 years of operation. These can deposit of order 1.5 m of snow in periods of 24 hours or less. On various occasions, these have not only closed the observatory, but also trapped personnel onsite with no means of escape. The OAN-SPM is the only organization in the area (and one of only two in the state) with snow removal equipment.

These storms inevitably arrive from the Pacific Ocean and their existence is known days in advance. However, their exact paths are much more uncertain, and it may be impossible to decide whether to evacuate until the day before the storm hits. In the most recent cases, in 1998 and 2010, the weather predictions were good enough from several days to a week before the storms hit to know that an unusually heavy snowfall (or precipitation) was imminent and that some action must be taken. What has proven most feasible in these cases is to prepare the installations by taking the telescopes and instruments out of operation and warming them to ambient temperature, draining pipes (most are actually rubber tubing at the OAN-SPM's three telescopes), shutting off generators, etc., and then evacuating both personnel and snow removal equipment before a storm hits. The experience with trapped personnel indicates that evacuation is much safer and much better for their morale. Once the storm passes, the roads are cleared, the personnel return, and the installations are brought online again. The road is usually opened in less than a week (it is harder to remove snow going uphill rather than down, as is normally done). The head of the OAN-SPM has taken these decisions. The return to operations can be delayed significantly due to the precipitation that falls as rain at altitudes lower than the observatory, which can cause flooding that has occasionally taken out bridges on the transpeninsular highway. Access to the OAN-SPM is only possible once such collateral damage has been repaired. Typically, access to the OAN-SPM is restored within two weeks of evacuation.

7. ASTROCLIMATE

In this section, we will consider the factors that are particularly crucial to a good observing site. In particular, we shall consider cloud cover, seeing and related issues, sky brightness, and precipitable water vapour.

7.1 Time available at night

At the latitude of the OAN-SPM, there are 4319 hours per year between sunset and sunrise and each of civil, nautical, and astronomical twilights represent about 1 hour each day[1]. Therefore, excluding civil and nautical twilight, there are up to 3589 hours available yearly for astronomical observations and calibrations under skies that are at least nearly dark. That figure does not account for time lost to weather, which is likely to be about 20% (§7.2), leaving approximately 2871 hours yearly.

7.2 Cloud cover

Since the fraction of clear nights was one of the factors considered when choosing the current location of the OAN, it should not be surprising that the OAN-SPM has a large fraction of clear nights. This was first studied by Mendoza (1971), but was continued very systematically by Tapia (1992, 2003) and Tapia et al. (2007). The three latter studies are based upon the records kept by the telescope operators at the 2.1m telescope and so reflect the fraction of time actually used for observation.

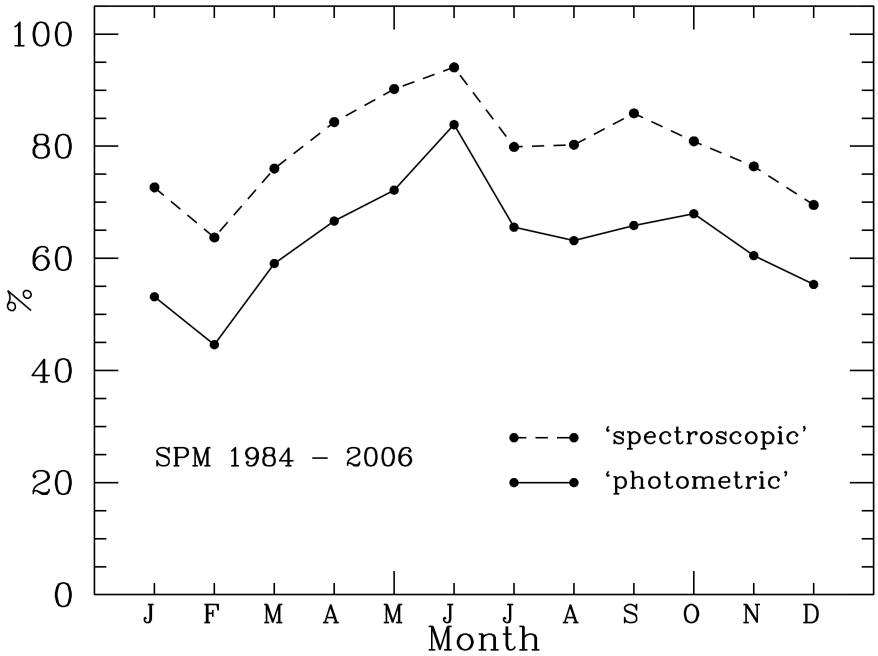

Figure 20: Monthly fraction of nights of photometric and spectroscopic quality in San Pedro Mártir during the period January 1983 to December 2006. (Figure and caption from Tapia et al. 2007)

Figure 20 presents the fraction of nights deemed photometric and spectroscopic over the 24 year period covering 1983 to 2006. April to October are definitely the best months while February is

[1] http://aa.usno.navy.mil/data/docs/RS_OneYear.php

clearly the worst by far. This seasonal variation is primarily a result of winter being the rainy season in southern California and the northern part of the Baja California peninsula. The dip in July-September reflects the monsoon-type clouds that cause afternoon rains during these months.

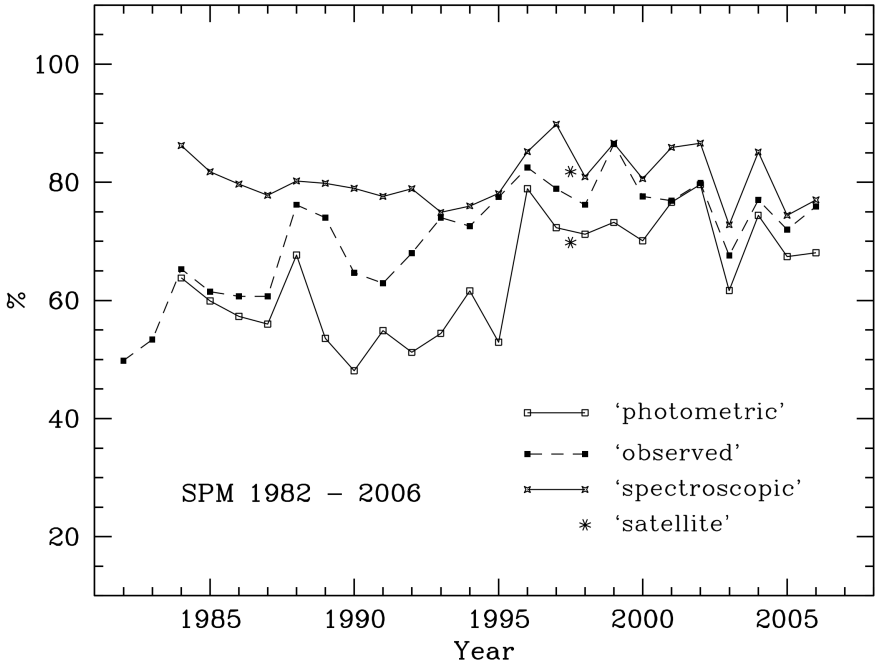

Figure 21: Yearly fraction of nights of photometric and spectroscopic quality in San Pedro Mártir during the period January 1984 - December 2006. Also shown is the actual use of the 2.1-m telescope from July 1982 to December 2006. The asterisks refer to the mean satellite June 1997-May 1998 measurements by Erasmus & van Staden (2002). (Figure and caption from Tapia et al. 2007)

Figure 21 shows the evolution of the fraction of photometric and spectroscopic nights over the same 24 year period. While the fraction of spectroscopic nights is relatively constant in the neighbourhood of 80%, there is a notable change in the fraction of photometric nights, from approximately 60% prior to 1995 to about 70% since then. This difference is likely correlated with the lower rainfall recorded in the region since 1995 (Tapia et al. 2007). These results agree with the study by Erasmus & van Staden (2002) based upon satellite data.

7.3 Seeing and atmospheric turbulence

The most recent study of seeing at the OAN-SPM is that done by the TMT site selection group (Skidmore et al. 2009). Their main results are shown in the four panels in Figure 22. On average (taking the behaviour of the median as indicative), they find that the seeing is relatively constant during the first six hours after sunset, but degrades thereafter until sunrise. Over the course of the year, they find that the best seeing occurs during summer and the worst in winter. The best seeing occurs in August-September when the seeing distribution is particularly narrow, with the 90th

percentile of the distribution near 1". They find that the seeing does not depend significantly upon the wind direction, but it is dependent upon the wind speed. The best seeing occurs for the lowest wind speeds, which occur in summer, on average. The median seeing reported by Skidmore et al. (2009) is 0.79" at 5000Å. The 10th percentile seeing at the same wavelength is 0.5".

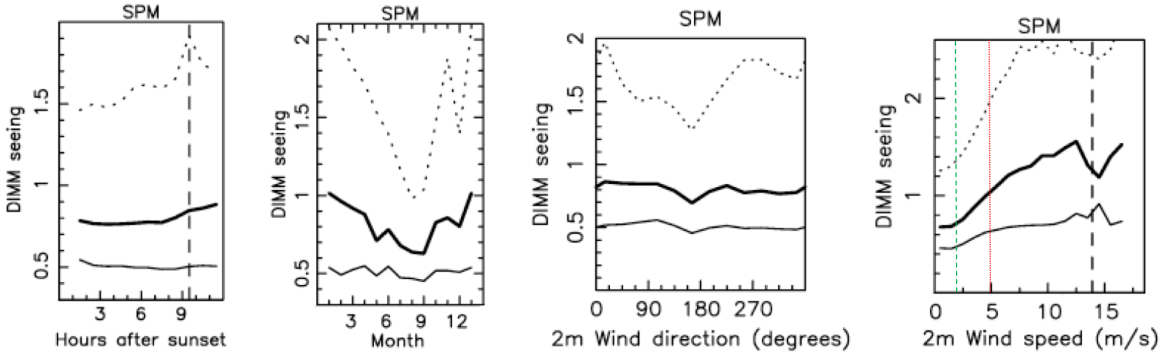

Figure 22: The four panels present the variation of the DIMM seeing measured by Skidmore et al. (2009) as a function of various variables. In all panels, the thin line represents the 10th percentile of the distribution, the thick line the median value, and the dotted line the 90th percentile of the distribution. The first panel (left) shows that there is little variation of the seeing after sunset, but that it does degrade slightly towards sunrise. In this panel, the vertical dashed line indicates the length of the shortest night. The second panel (from left) indicates that the seeing is better in summer and worst in winter. From the third panel (from left), there is little variation in the seeing as a function of the wind's direction. However, the last panel (right) indicates that the seeing depends upon the wind speed, with the best seeing at low wind speeds. In this panel, the vertical dashed lines indicate the median wind speed measured (green), the 90-th percentile wind speed (red), and the telescope shutdown wind speed (black). All of these figures are adapted from Skidmore et al. (2009).

Similar results were obtained by Michel et al. (2003) concerning the seasonal variation of the distribution of the seeing. Their results are shown in Figure 23. They also find that the distribution of the seeing is narrowest and has the smallest median value in summer. In winter, the distribution is broader and its median value is larger. The distributions for spring and fall are intermediate between these extremes. Avila et al. (2004) found a similar median seeing, 0.71" in their case, but this was derived after correcting for a "dome seeing" contribution.

Figure 24 and Figure 25 summarize the knowledge of the atmospheric turbulence at the OAN-SPM (Echevarría et al. 1998; Sánchez et al. 2003; Skidmore et al. 2009), though other data are available (e.g., Avila et al. 1998, 2004). Close the the ground, it is known that the seeing improves significantly with height above a height of approximately 10 m (Echevarría et al. 1998; Sánchez et al. 2003). Both of the studies considered in Figure 24 were conducted at the TSPM site.

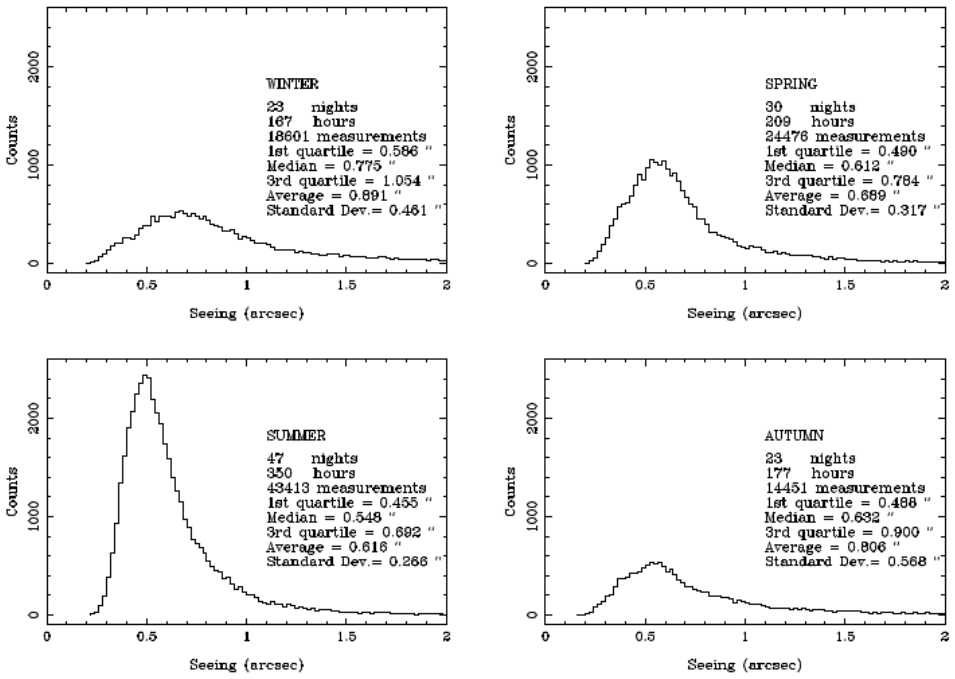

Figure 23: These four panels present the distributions of the seeing over the course of the year from Michel et al. (2003). As for the results of Skidmore et al. (2009), they find that the seeing is best in summer and worst in winter.

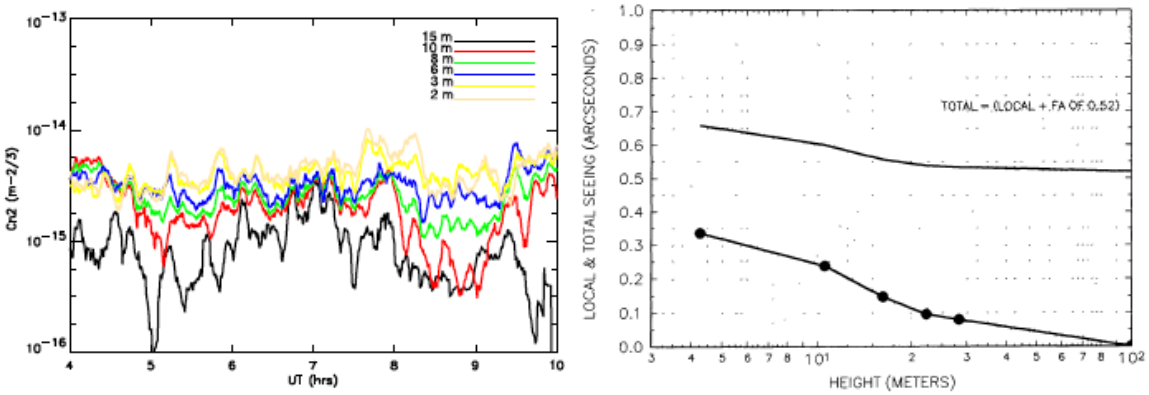

Figure 24: The left panel presents the temporal variation of the index of refraction structure constant C_n^2 during a typical night very near the ground from Sánchez et al. (2003). The different curves represent the contributions at different heights above the ground. A general result is that the strength of the fluctuations drops significantly between 10 m and 15 m above ground level. The right panel presents the seeing derived from the temperature structure constant as a function of height above the ground from Echevarría et al. (1998). Again, a strong decrease is noted above 10 m above the ground level.

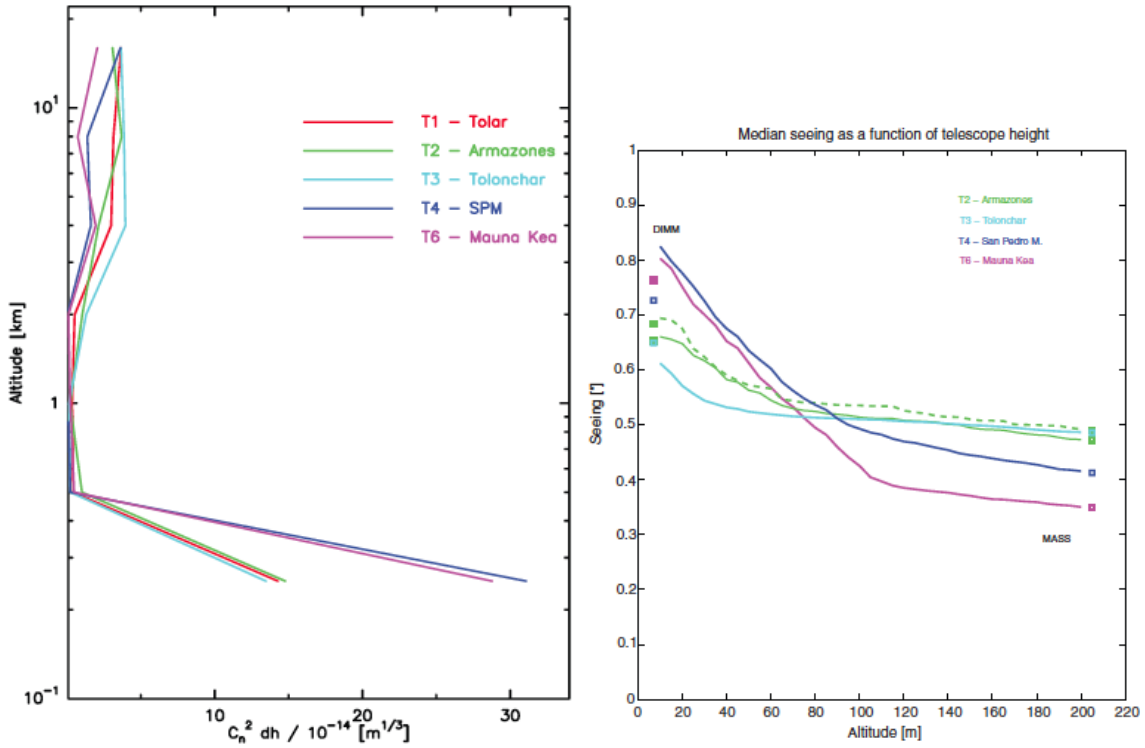

Figure 25: These figures are from the TMT site study (Schöck et al. 2009). In both panels, the dark blue curve is the data for the OAN-SPM. The left panel presents the mean index of refraction structure constant C_n^2 as a function of height above the ground. The dominant layer above the OAN-SPM is clearly the ground layer. The right panel considers effects much closer to the ground, and indicates how strongly the layers closest to the ground affect the seeing.

Figure 25 indicates that the rate of improvement in seeing near the ground continues rapidly to heights of approximately 100 m (Skidmore et al. 2009). From that point, the rate improvement slows. Considering the whole atmosphere, the dominant contributor to the total seeing is the ground layer (see also Avila et al. 1998, 2004). The next important contribution occurs in the free atmosphere, at an altitude of 4km. Els et al. (2009) provide an in-depth discussion of the turbulence profile above the OAN-SPM, based upon data obtained at the TSPM site. An important consequence of these results is that the seeing is not expected to vary strongly from site-to-site in the vicinity of the TSPM site. Indeed, Bohigas et al. (2008) found just this result over a much larger area, based upon in-situ measurements at five neighbouring sites. The differences they found were at the level of systematic uncertainties in their study, which they undertook in summer and fall. They infer that the similarities in terms of seeing, wind speed, temperature, and humidity implies that the ground layer turbulence is not strongly influenced by the very local topography, including the presence of trees. This is perhaps not unexpected if its thickness is of approximately 100 m, as found from the TMT studies.

Measurements of the isoplanatic angle are available from Avila et al. (2004) and the TMT site testing group (Skidmore et al. 2009). The former finds a median value of 1.87" ± 0.04" while the latter finds 2.03".

7.4 Atmospheric extinction

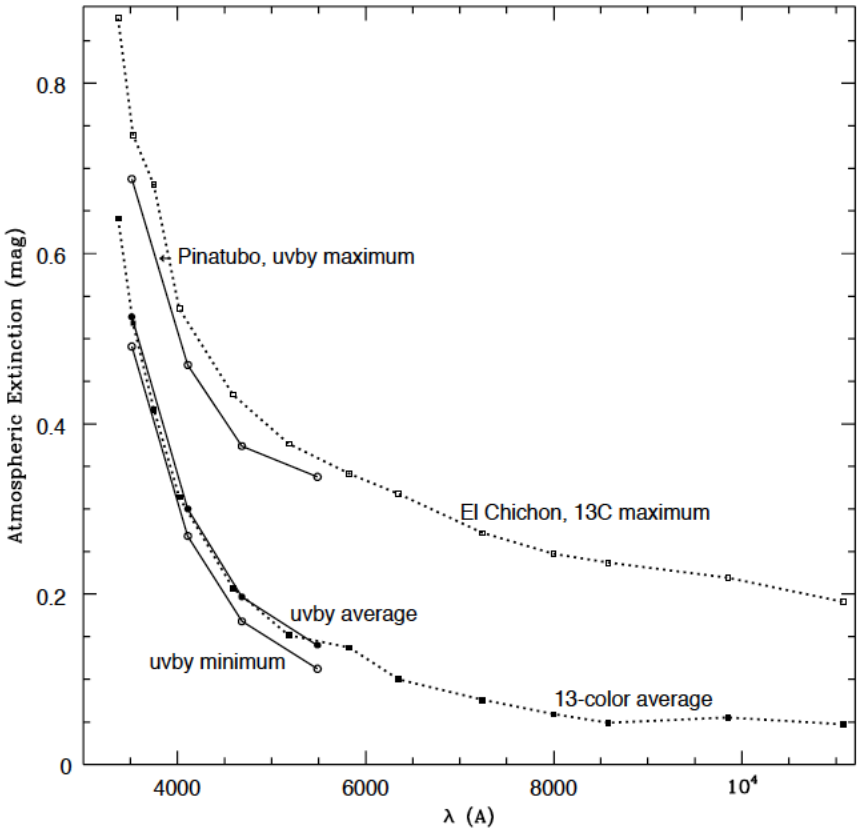

Figure 26: Atmospheric extinction versus the equivalent wavelengths of the 13C and 4-color filters. Solid squares and circles show the average extinctions from 151(8C)/120(6RC) nights of 13C photometry and 158(mags.)/182(colors) nights of 4-color photometry, respectively. The lowest curve shows the "minimum" 4-color extinction as derived from 12 nights with optimal, stable conditions from 6 good observing runs from 1988 through 1998. These mean and minimum values are shown in Table 1. The highest curves of this graph show the maximum effects caused by volcanic aerosols, the night of 19/20 Jun'82 for 13C photometry and the El Chichón volcano (open squares), and the night of 4/5 May'92 for 4-colors and Pinatubo (open circles). (Figure and caption from Schuster & Parrao 2001)

By far, the most detailed study of the atmospheric extinction at the OAN-SPM is that of Schuster & Parrao (2001). This study is based upon 13-colour photometry obtained on 294 nights over the decade 1973-1983 and *uvby* photometry obtained during 272 nights from 1984 to 1999. The agreement between the two data sets over the wavelength interval in common is excellent (see Figure 26), while the wavelength coverage of the 13-colour photometry extends from the near-ultraviolet to the near-infrared. Figure 27 presents the cumulative distribution of the y-band

extinction coefficient, k_y (Schuster et al. 2002), considering the entire *uvby* data set (245 nights; 1984 to 1999) and the data set excluding the period affected by dust from the Pinatubo volcano (173 nights; Oct. 1991 to Apr. 1994). Excluding the nights affected by the dust from the Pinatubo volcano, the mean atmospheric extinction in the *y* filter is 0.14 mag/airmass at an effective wavelength of 5488Å (median value 0.131 mag/airmass) and 91% of all nights have extinction coefficientes below 0.17 mag/airmass. Considering all measurements, the median extinction in the *y* filter is 0.145 mag/airmass.

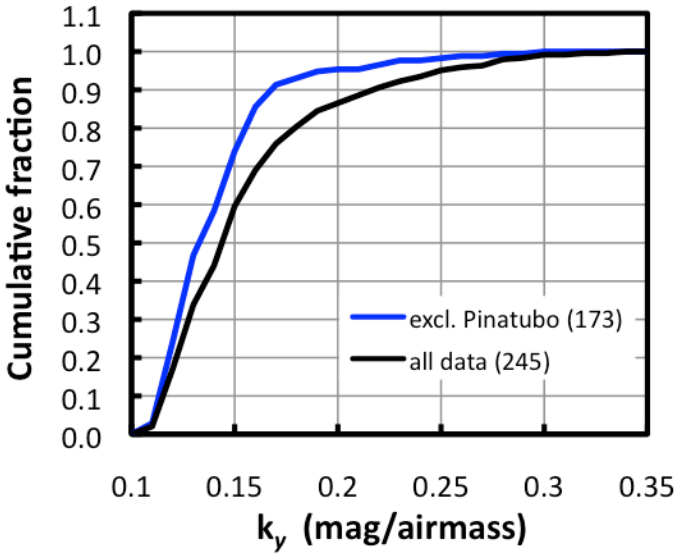

Figure 27: This plot presents the cumulative distribution of y-band extinction coefficients from Schuster et al. (2002). The data are plotted including and excluding the period during which the Pinatubo volcano's dust affected the atmosphere worldwide (Oct. 1991 to April 1994) since this dust is not part of the OAN-SPM's normal environment. The numbers in parentheses indicate the number of nights in each data set.

In the near-infrared, the JHK extinction coefficients remain low, e.g., Carrasco et al. (1991) report values of 0.092 mag, 0.032 mag, and 0.045 mag in J, H, and K, respectively.

7.5 Sky brightness

Light pollution was one of the factors that were explicitly considered when choosing the current site of the OAN in the 1960s, so, again, it is not surprising that the OAN-SPM has very dark skies.

Mendoza (1971) is the first to report sky brightness measurements, of 22 mag/□" and 23 mag/□" in the V- and B-bands, respectively, measured in February-March 1971. Tapia et al. (2007) report 21.5 mag/□" and 22.4 mag/□" in the V- and B-bands, respectively, measured between August 2004 and February 2006. More recently, Plauchu-Frayn et al. (2016) find a sky brightness, corrected for zodiacal light and excluding measurements near the Galactic plane, of 21.84 mag/□" in V-band and 23.10 mag/□" in B-band for measurements made between February 2013 and May

2016. They show that these values are similar to the sky brightness found at other dark sites at similar phases of the solar activity cycle. Since the peak of the current solar activity cycle, Plauchu-Frayn et al. (2016) find that the sky brightness has increased by ΔU=0.7, ΔB=0.5, ΔV=0.3, and ΔR=0.5 mag/□". The maximum variation over a solar cycle is expected to be about 2-3 times the change found for the current cycle, depending upon the bandpass.

In the infrared, zenith sky brightnesses of 16.0-16.9 mag/□" and 14.1 mag/□" were measured in J- and H-band in March 2005, respectively. In K'-band, sky brightnesses of 14.4-15.0 mag/□" and 13.6-14.0 mag/□" were measured in March 2005 and May 2006, respectively (Tapia et al. 2007). The brighter sky background in K'-band in May 2006 probably indicates a higher thermal emission from the atmosphere for these observations and, more generally, a likely seasonal variation in the thermal infrared sky brightness. The sky brightness at La Palma, at a similar latitude, has a similar behaviour (Sánchez et al. 2008).

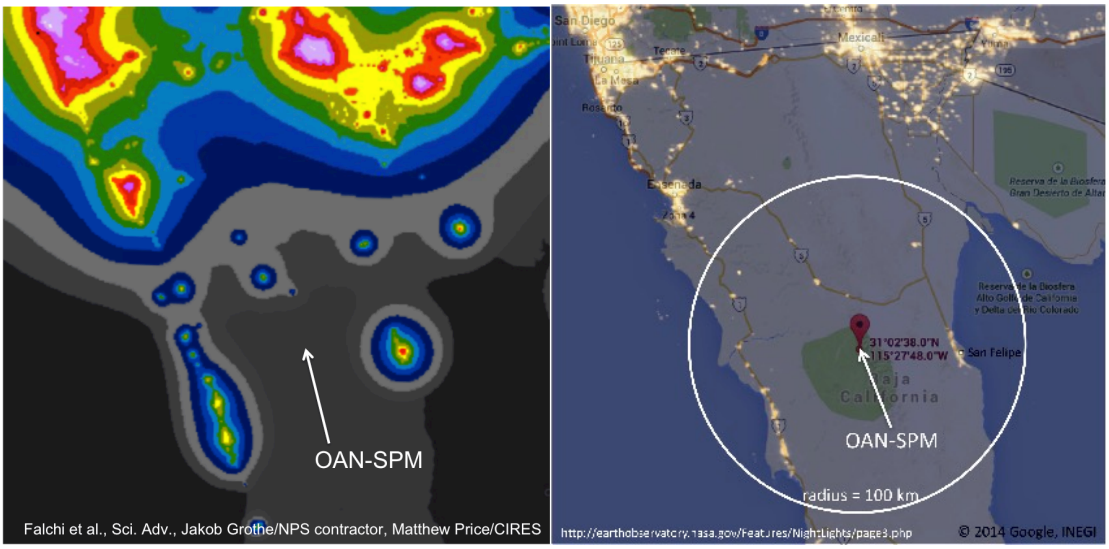

Figure 28: On the left is the most recent light pollution map generated by Falchi et al. (2016, Science Advances, 2, e1600377; DOI: 10.1126/sciadv.1600377). According to this study, the light pollution OAN-SPM is less than 1% of the natural night sky brightness. On the right, the area covering northern Baja California from the 2012 NASA Earth Observatory map of the Earth at night is superposed upon a Google Earth map of the same area.

Figure 28 presents the most recent light pollution map generated by Falchi et al. (2016). This map indicates that the light pollution at the OAN-SPM falls within their lowest band, less than 1% of the natural sky brightness at the site.

Given the motivation to locate the OAN at SPM, the OAN-SPM has for a long time advocated for lighting ordnances in order to keep the sky in SPM dark. The first legislation to this end took effect in the municipality of Ensenada in 2006. State-wide legislation came into effect in early 2010 as a result of efforts during the International Year of Astronomy in 2009. In both cases, the legislation

is included as part of the environmental protection and seeks to minimize light pollution and the natural and economic resources devoted to outdoor lighting. So far, the focus has been on street lights, but more recently electronic billboards have been included. In principle, all aspects of outdoor lighting could fall under its jurisdiction, a result that could enhance public safety in a number of areas.

7.6 Precipitable water vapour

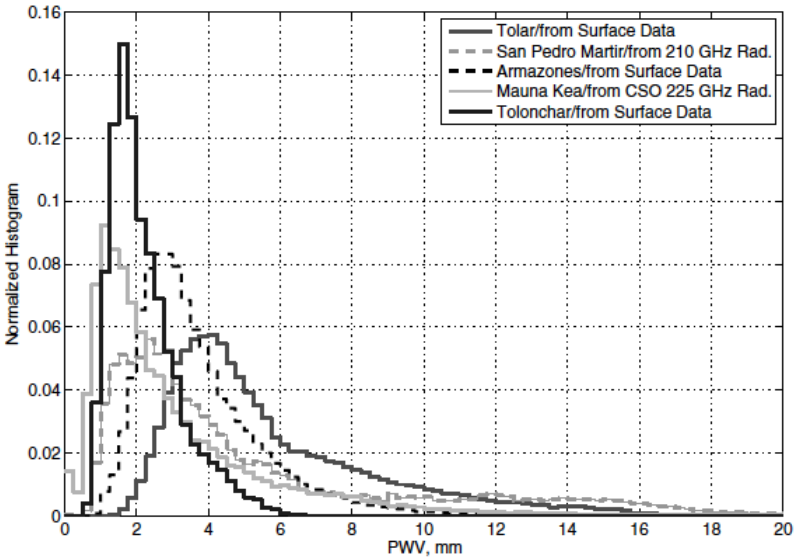

Table 6: PWV values (mm) from Otárola et al. (2010).

Season	Q1	median
Summer	4.0	7.9
Fall	2.3	3.7
Winter	1.3	2.2
Spring	2.2	3.1
Yearly	2.1	3.4

Figure 29: The normalized histogram of PWV measurements from Otárola et al. (2010). The secondary peak of PWV measurements for SPM is due to the summer monsoon that affects the summer especially and the fall to a lesser extent (Table 6). The winter and spring seasons are considerably drier.

Figure 29 and Table 6 present the results of the precipitable water vapour (PWV) measurements made as part of the TMT site characterization study (Otárola et al. 2010). Table 6 presents the 25th percentile and median values of the distribution. These measurements cover the year 2006 (see Otárola et al. 2009 for details) and are based upon the same equipment described in Hiriart et al. (2003) and for the results summarized by Hiriart (2003). Figure 30 presents the monthly means averaged over the years 1995-2002 and the yearly averages over the same time period from Hiriart (2003). These results show very clearly how the "wet" period from July to September is very different from the rest of the year as regards the PWV at SPM. For reference, the median value of the PWV reported by Hiriart (2003) for the period 1995-2002 is similar to that reported in Table 6.

Prior to the above studies, PWV measurements had been reported by Mendoza (1971) as well as Alvarez & Maisterrena (1977). Mendoza (1971) provides few details regarding the instrument used, but reports 81% of the measurements fall between values of 1 mm and 3 mm. On the other hand, Alvarez & Maisterrena (1977) report measurements attributed to Westphal (1974) and report

a mean PWV of 3.3 mm. Hence, it would appear that the yearly mean value from Table 6 is a representative value.

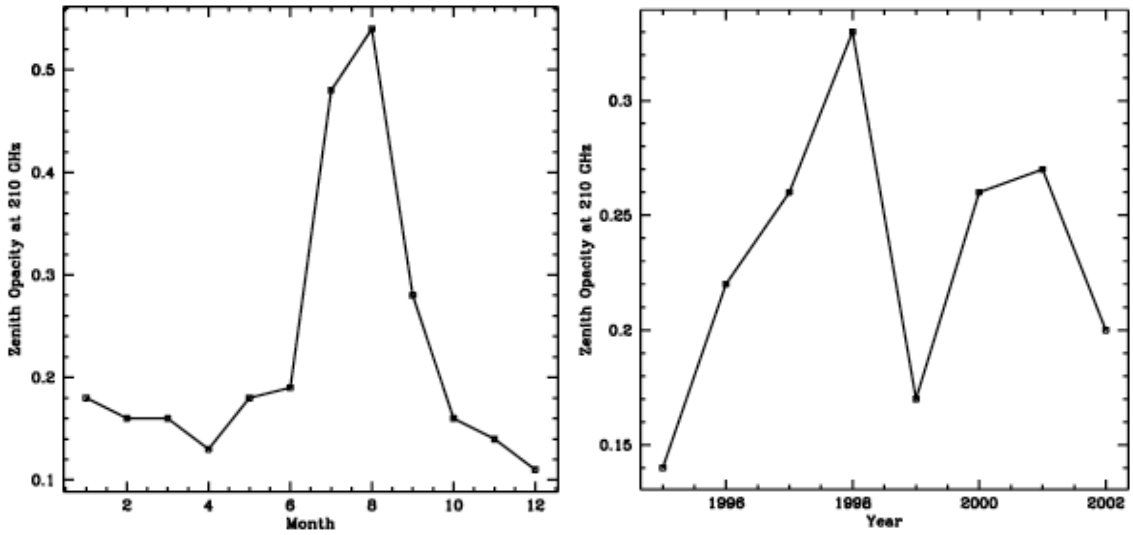

Figure 30: These panels present the monthly (left) and yearly mean opacity at 210 GHz reported by Hiriart (2003). The summer monsoon (July-September) is the obvious anomaly in the seasonal statistics. There are also significant year-to-year effects, such as the "El Niño" event in 1998. The zenith opacity reported here may be converted to PWV in mm via PWV = 19.46 τ_{210GHz} - 0.3062 (Otárola et al 2009).

8. THE SPECIFIC TSPM SITE

Figure 31 shows the area covered by the geotechnical study undertaken by the Gerencia de Ingeniería Civil, a specialized branch of the Comisión Federal de Electricidad (CFE) in late 2015. This study incorporates the data from the field campaigns from 2001 and 2015. The purpose of this study was to determine the structure of the subsoil where the TSPM is to be built. The following studies were undertaken, the results of which may be found in the CFE's final report (nearly 500 pages).

- Topographic surveying
- Survey of the site's geology and geological structure
- Seismic refraction tomography
- Borehole seismic tomography
- Surface wave dispersion tomography
- Electrical resistance tomography
- Transient electromagnetic sounding
- Site specific seismic hazard analysis
- The soil's electrical resistivity and corrosivity
- Study of the proposed foundations
- Recommendations for road construction

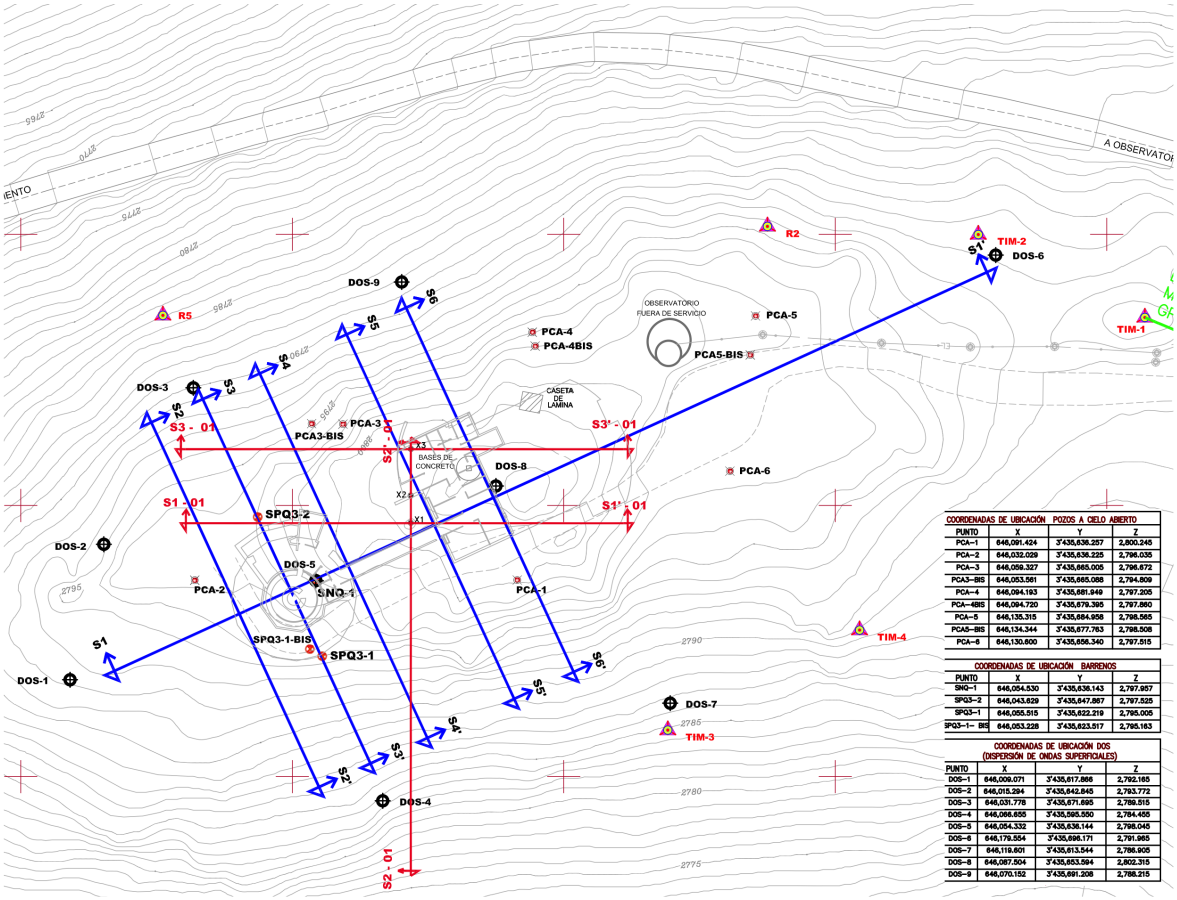

COORDENADAS DE UBICACIÓN POZOS A CIELO ABIERTO

PUNTO	X	Y	Z
PCA-1	646,091.424	3'435,636.257	2,800.245
PCA-2	646,032.029	3'435,636.225	2,796.035
PCA-3	646,050.327	3'435,665.005	2,796.672
PCA3-BIS	646,053.581	3'435,665.088	2,794.809
PCA-4	646,094.193	3'435,681.949	2,797.205
PCA-4BIS	646,094.720	3'435,679.395	2,797.880
PCA-5	646,135.315	3'435,684.958	2,798.565
PCA5-BIS	646,134.344	3'435,677.763	2,798.508
PCA-6	646,130.600	3'435,656.340	2,797.515

COORDENADAS DE UBICACIÓN BARRENOS

PUNTO	X	Y	Z
SNQ-1	646,054.530	3'435,636.143	2,797.957
SPQ3-2	646,043.829	3'435,647.887	2,797.525
SPQ3-1	646,055.515	3'435,622.219	2,795.005
SPQ3-1- BIS	646,053.228	3'435,623.517	2,795.163

COORDENADAS DE UBICACIÓN DOS (DISPERSIÓN DE ONDAS SUPERFICIALES)

PUNTO	X	Y	Z
DOS-1	646,009.071	3'435,617.866	2,792.185
DOS-2	646,015.294	3'435,642.845	2,793.772
DOS-3	646,031.778	3'435,671.695	2,786.515
DOS-4	646,066.655	3'435,595.550	2,784.455
DOS-5	646,054.332	3'435,636.144	2,795.045
DOS-6	646,179.554	3'435,696.171	2,791.965
DOS-7	646,119.601	3'435,613.544	2,786.905
DOS-8	646,087.504	3'435,653.594	2,802.315
DOS-9	646,070.152	3'435,691.208	2,788.215

Figure 31: This map shows the area studied by the CFE geotechnical studies from 2001 (red lines) and 2016 (blue lines and black labels). The red triangles are the reference points for the 2016 topographical map. The UTM coordinates of the black symbols, e.g., DOS-1, are given in the table. These points are referenced in Figure 32 and Figure 33. Also shown are outlines of the ground floor of the TSPM telescope enclosure and of the support building as well as other existing buildings at this site.

8.1 Geographic coordinates

The geographic coordinates of the centre of the telescope pier are given in Table 7. These coordinates were derived by first measuring the coordinates of the the centre of the pier and the points SNQ-1, SPQ3-2, SPQ3-1, and SPQ3-1-BIS shown in Figure 31 from the topographic map from which Figure 31 was generated (file: kg4alatcop0001a topo.dwg). These cartesian coordinates were then mapped to the UTM coordinates for these points shown in the table in Figure 31. From this mapping, the UTM coordinates of the centre of the pier were derived. To derive the latitude and longitude coordinates of the centre of the pier, a mapping between the geodesic and UTM coordinates for the points MOJONERA-1, R2, R3, and R5 from Table II.6 of the CFE's final geotechnical report was used. (R2 and R5 are shown in Figure 31. R3 is not shown, but nearly

coincides with DOS-7 in Figure 31. MOJONERA-1 is well off the map in Figure 31.) The UTM coordinates used in the CFE's report are in the system UTM zone 11 ITRF-08 epoch 2010.0.

Table 7: Geographic coordinates of the telescope pier.

	Geodesic coordinates		UTM coordinates[a]	
	longitude (W)	**latitude (N)**	**x**	**y**
telescope pier	115º 28' 10.16"	31º 02' 43.15"	646050.336	3435632.849

[a] The system is UTM zone 11 ITRF-08 epoch 2010.0.

8.2 Geophysical nature

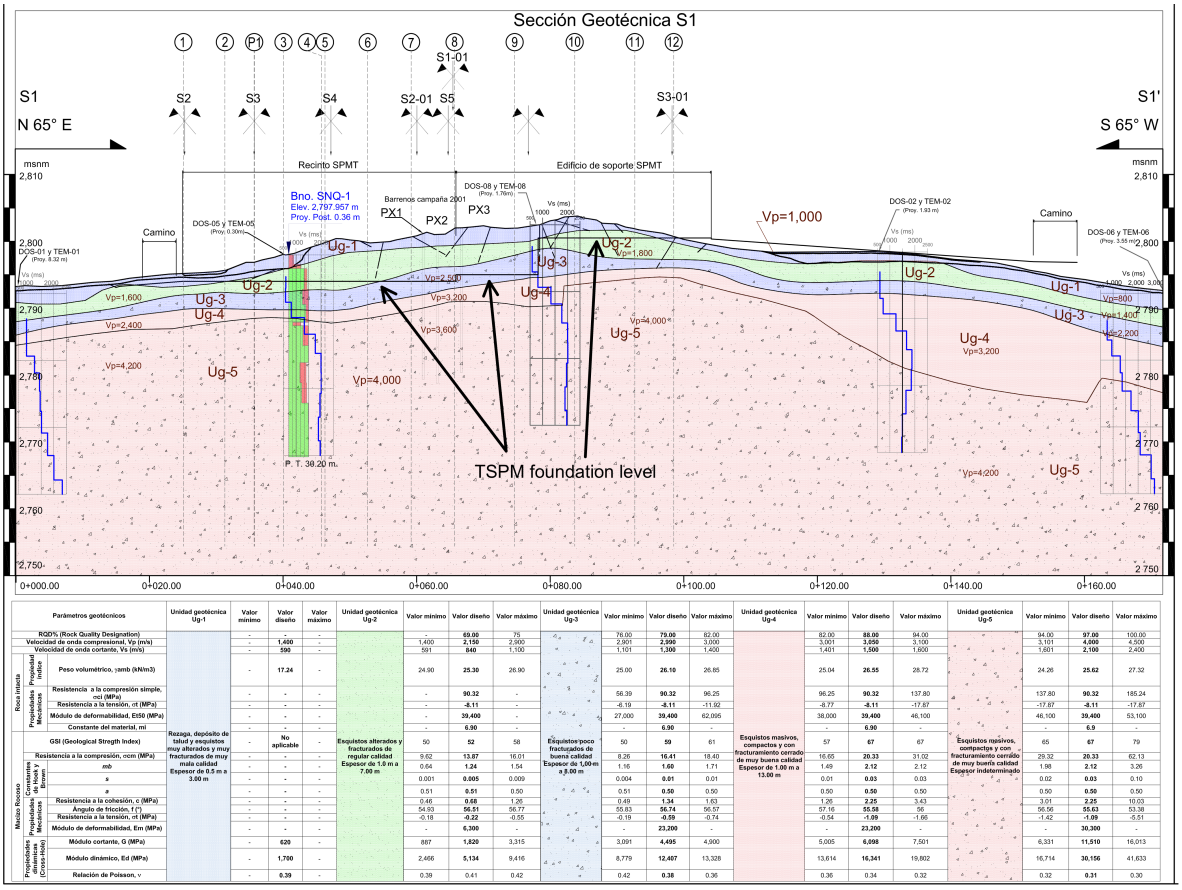

Parámetros geotécnicos	Unidad geotécnica Ug-1	Valor mínimo	Valor diseño	Valor máximo	Unidad geotécnica Ug-2	Valor mínimo	Valor diseño	Valor máximo	Unidad geotécnica Ug-3	Valor mínimo	Valor diseño	Valor máximo	Unidad geotécnica Ug-4	Valor mínimo	Valor diseño	Valor máximo	Unidad geotécnica Ug-5	Valor mínimo	Valor diseño	Valor máximo
RQD% (Rock Quality Designation)	Rezaga, depósito de talud y esquistos muy alterados y muy fracturados de muy mala calidad Espesor de 0.5 m a 3.00 m	-	-	-	Esquistos alterados y fracturados de regular calidad Espesor de 1.0 m a 7.00 m	-	**69.00**	75	Esquistos poco fracturados de buena calidad Espesor de 1,00 m a 8.00 m	76.00	**79.00**	82.00	Esquistos masivos, compactos y con fracturamiento cerrado de muy buena calidad Espesor de 1.00 m a 13.00 m	82.00	**88.00**	94.00	Esquistos masivos, compactos y con fracturamiento cerrado de muy buena calidad Espesor indeterminado	94.00	**97.00**	100.00
Velocidad de onda compresional, Vp (m/s)		-	**1,400**	-		1,400	**2,150**	2,900		2,901	**2,950**	3,000		3,001	**3,050**	3,100		3,101	**4,000**	4,500
Velocidad de onda cortante, Vs (m/s)		-	**590**	-		591	**840**	1,100		1,101	**1,300**	1,400		1,401	**1,500**	1,800		1,801	**2,100**	2,400
Roca intacta – Propiedad índice: Peso volumétrico, γamb (kN/m3)		-	**17.24**	-		24.90	**25.30**	26.90		25.00	**26.10**	26.85		25.04	**26.55**	28.72		24.26	**25.62**	27.32
Roca intacta – Propiedades mecánicas: Resistencia a la compresión simple, σci (MPa)		-	-	-		-	**90.32**	-		56.39	**90.32**	96.25		96.25	**90.32**	137.80		137.80	**90.32**	185.24
Roca intacta – Propiedades mecánicas: Resistencia a la tensión, σt (MPa)		-	-	-		-	**-8.11**	-		-8.19	**-8.11**	-11.92		-8.77	**-8.11**	-17.87		-17.87	**-8.11**	-17.87
Roca intacta – Propiedades mecánicas: Módulo de deformabilidad, Ei50 (MPa)		-	-	-		-	**39,400**	-		27,000	**39,400**	62,095		38,000	**39,400**	46,100		46,100	**39,400**	53,100
Roca intacta – Propiedades mecánicas: Constante del material, mi		-	-	-		-	**6.90**	-		-	**6.90**	-		-	**6.90**	-		-	**6.9**	-
Macizo Rocoso – Clasificación geomecánica de Hoek y Brown: GSI (Geological Stregth Index)		-	**No aplicable**	-		50	**52**	58		50	**59**	61		57	**67**	67		65	**67**	79
Macizo Rocoso – Clasificación geomecánica de Hoek y Brown: Resistencia a la compresión, σcm (MPa)		-	-	-		9.62	**13.87**	16.01		8.26	**16.41**	18.46		16.65	**20.33**	31.02		29.32	**20.33**	62.13
Macizo Rocoso – Clasificación geomecánica de Hoek y Brown: mb		-	-	-		0.64	**1.24**	1.54		1.16	**1.60**	1.71		1.49	**2.12**	2.12		1.98	**2.12**	3.26
Macizo Rocoso – Clasificación geomecánica de Hoek y Brown: s		-	-	-		0.001	**0.005**	0.009		0.004	**0.01**	0.01		0.01	**0.03**	0.03		0.02	**0.03**	0.10
Macizo Rocoso – Clasificación geomecánica de Hoek y Brown: a		-	-	-		0.51	**0.51**	0.50		0.51	**0.50**	0.50		0.50	**0.50**	0.50		0.50	**0.50**	0.50
Macizo Rocoso – Propiedades mecánicas: Resistencia a la cohesión, c (MPa)		-	-	-		0.46	**0.68**	1.26		0.49	**1.34**	1.63		1.26	**2.25**	3.43		3.01	**2.25**	10.03
Macizo Rocoso – Propiedades mecánicas: Angulo de fricción, f (°)		-	-	-		54.93	**56.51**	56.77		55.83	**56.74**	56.57		57.16	**55.58**	56		56.56	**55.63**	53.38
Macizo Rocoso – Propiedades mecánicas: Resistencia a la tensión, σt (MPa)		-	-	-		-0.18	**-0.22**	-0.55		-0.19	**-0.59**	-0.74		-0.54	**-1.09**	-1.66		-1.42	**-1.09**	-0.51
Macizo Rocoso – Propiedades mecánicas: Módulo de deformabilidad, Em (MPa)		-	-	-		-	**6,300**	-		-	**23,200**	-		-	**23,200**	-		-	**30,300**	-
Propiedades dinámicas (Cross-Hole): Módulo cortante, G (MPa)		-	**620**	-		887	**1,820**	3,315		3,091	**4,495**	4,900		5,005	**6,098**	7,501		6,331	**11,510**	16,013
Propiedades dinámicas (Cross-Hole): Módulo dinámico, Ed (MPa)		-	**1,700**	-		2,466	**5,134**	9,416		8,779	**12,407**	13,328		13,614	**16,341**	19,802		16,714	**30,156**	41,633
Relación de Poisson, ν		-	**0.39**	-		0.39	0.41	0.42		0.42	**0.38**	0.36		0.36	0.34	0.32		0.32	**0.31**	0.30

Figure 32: This figure presents the geological structure and its properties as a function of depth along the section S1 from Figure 31. The seismic P-wave velocities are given at different points while the variation of the S-wave velocities with depth are shown at 5 points along the section (see Figure 31 for the identifiers). The table (requires a magnifying glass) provides details of other physical parameters. The positions of the telescope enclosure (Recinto SPMT), support building (Edificio de soporte SPMT), and the road (Camino) are shown. The proposed foundation levels are shown as the straight horizontal lines.

The soil structure at the TSPM site consists of four layers of rock that sit atop a very thick base layer whose total thickness was not reached by the 30 m depth probed in these studies. The surface

layer in most places is rubble. It is a thin layer and is absent in some places. This layer will be removed for construction. Underlying the surface layer are three layers of successively denser and less fractured rock. All three are relatively thin, though the deepest reaches a thickness of 13m in the northeast corner of the map shown in Figure 31. The base layer is the densest and least fractured of all.

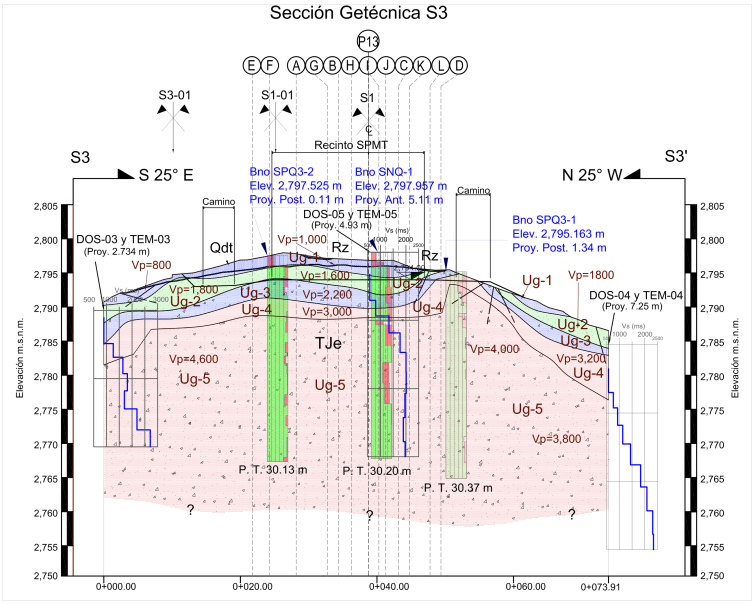

Parámetros geotécnicos		Unidad geotécnica Ug-1	Valor mínimo	Valor diseño	Valor máximo	Unidad geotécnica Ug-2	Valor mínimo	Valor diseño	Valor máximo	Unidad geotécnica Ug-3	Valor mínimo	Valor diseño	Valor máximo	Unidad geotécnica Ug-4	Valor mínimo	Valor diseño	Valor máximo	Unidad geotécnica Ug-5	Valor mínimo	Valor diseño	Valor máximo
RQD% (Rock Quality Designation)		Rezaga, depósito de talud y esquistos muy alterados y muy fracturados de muy mala calidad Espesor de 0.5 m a 3.00 m	-	-	-	Esquistos alterados y fracturados de regular calidad Espesor de 1.0 m a 7.00 m	-	69.00	75	Esquistos poco fracturados de buena calidad Espesor de 1.00 m a 9.00 m	76.00	79.00	82.00	Esquistos masivos, compactos y con fracturamiento cerrado de muy buena calidad Espesor de 1.00 m a 13.00 m	82.00	88.00	94.00	Esquistos masivos, compactos y con fracturamiento cerrado de muy buena calidad Espesor indeterminado	94.00	97.00	100.00
Velocidad de onda compresional, Vp (m/s)			-	1,400	-		1,400	2,150	2,900		2,901	2,990	3,000		3,001	3,050	3,100		3,101	4,000	4,500
Velocidad de onda cortante, Vs (m/s)			-	550	-		591	840	1,100		1,101	1,300	1,400		1,401	1,500	1,600		1,801	2,100	2,400
Roca intacta — Propiedades Índice	Peso volumétrico, γamb (kN/m3)		-	17.24	-		24.90	25.30	26.90		25.00	26.10	26.85		25.04	26.55	28.72		24.26	25.62	27.32
Roca intacta — Propiedades Mecánicas	Resistencia a la compresión simple, σci (MPa)		-	-	-		-	90.32	-		56.39	90.32	96.25		96.25	90.32	137.80		137.80	90.32	185.24
	Resistencia a la tensión, σt (MPa)		-	-	-		-	-8.11	-		-6.19	-8.11	-11.92		-8.77	-8.11	-17.87		-17.87	-8.11	-17.87
	Módulo de deformabilidad, Eti50 (MPa)		-	-	-		-	39,400	-		27,000	39,400	62,095		38,000	39,400	46,100		46,100	39,400	53,100
	Constante del material, mi		-	-	-		-	6.90	-		-	6.90	-		-	6.90	-		-	6.9	-
Macizo Rocoso — Constantes de Hoek y Brown	GSI (Geological Streath Index)		-	No aplicable	-		50	52	58		50	59	61		57	67	67		65	67	79
	Resistencia a la compresión, σcm (MPa)		-	-	-		9.62	13.87	16.01		8.26	16.41	18.40		16.65	20.33	31.02		29.32	20.33	62.13
	mb		-	-	-		0.64	1.24	1.54		1.16	1.60	1.71		1.49	2.12	2.12		1.98	2.12	3.26
	s		-	-	-		0.001	0.005	0.009		0.004	0.01	0.01		0.01	0.03	0.03		0.02	0.03	0.10
	a		-	-	-		0.51	0.51	0.50		0.51	0.50	0.50		0.50	0.50	0.50		0.50	0.50	0.50
Macizo Rocoso — Propiedades Mecánicas	Resistencia a la cohesión, c (MPa)		-	-	-		0.46	0.68	1.26		0.49	1.34	1.63		1.26	2.25	3.43		3.01	2.25	10.03
	Ángulo de fricción, f (°)		-	-	-		54.93	56.51	56.77		55.83	56.74	56.57		57.16	55.58	56		56.56	55.63	53.38
	Resistencia a la tensión, σt (MPa)		-	-	-		-0.18	-0.22	-0.55		-0.19	-0.59	-0.74		-0.54	-1.09	-1.66		-1.42	-1.09	-5.51
	Módulo de deformabilidad, Em (MPa)		-	-	-		-	6,300	-		-	23,200	-		-	23,200	-		-	30,300	-
Propiedades dinámicas (Cross-Hole)	Módulo cortante, G (MPa)		-	620	-		887	1,820	3,315		3,091	4,495	4,900		5,005	6,098	7,501		6,331	11,510	16,013
	Módulo dinámico, Ed (MPa)		-	1,700	-		2,466	5,134	9,416		8,779	12,407	13,328		13,614	16,341	19,802		16,714	30,156	41,633
	Relación de Poisson, ν		-	0.39	-		0.39	0.41	0.42		0.42	0.38	0.36		0.36	0.34	0.32		0.32	0.31	0.30

Figure 33: This figure presents the geological structure and its properties as a function of depth along the section S3 from Figure 31 that goes through the pier of the telescope. The seismic P-wave velocities are given at different points while the variation of the S-wave velocities with depth are shown at 3 points along the section (see Figure 31 for the identifiers). The table (requires a magnifying glass) provides details of other physical parameters. The locations of the telescope enclosure (Recinto SPMT) and the road (Camino) are shown.

Figure 32 shows the subsoil structure along the section S1 shown in Figure 31. Also shown in this figure is the level of the TSPM foundations, which will require removal of the surface later over almost the entirety of this section, setting the foundation upon the good quality rock in the second or third layers. Only the very eastern end of the support building will be atop fill. Figure 33 shows similar information for the section S3 that cuts through what will be the telescope pier. Very

generally, the study concludes that the subsoil structure is a very suitable platform upon which to build the TSPM.

8.3 Seismic properties of the area

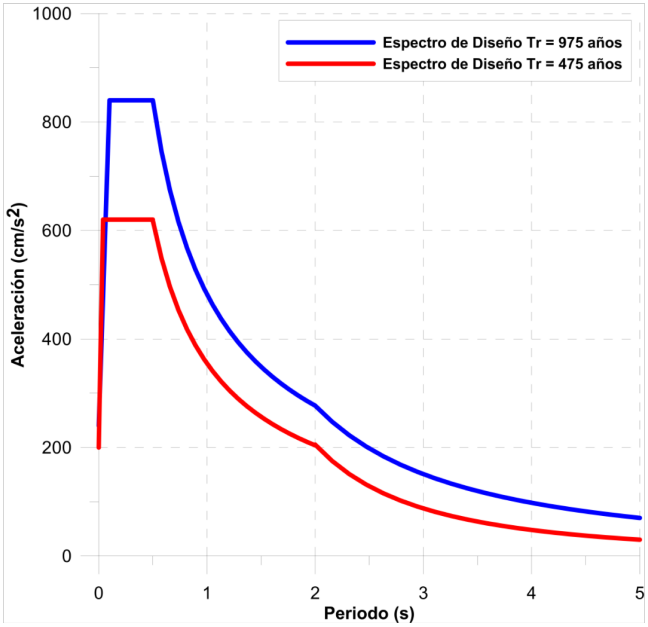

Figure 34: Design spectrum for return periods of 475 and 975 years with 5% damping. The units of the spectral acceleration are gals (1g = 980 gals). (This figure and Table 8 are from CFE's re-evaluation of the geotechnical study in July 2017.)

Table 8: CFE Seismic design spectrum for the TSPM project.

Acceleration (1 g = 980 gal)		**Period (s)**
(gal)	(g)	
$6000T + 240$	$6.12T + 0.245$	$0 < T < 0.1$ s
840	0.856	$0.1 < T < 0.5$ s
$480T^{-0.8}$	$0.489T^{-0.8}$	$0.5 < T < 2$ s
$785T^{-1.5}$	$0.800T^{-1.5}$	$T > 2.0$ s

Northern Baja California is crisscrossed by various fault systems, generally related to the interaction of the Pacific and North American tectonic plates. Although there has never been a strong earthquake at the OAN-SPM, they are not impossible and small earthquakes do occur. Several institutions maintain seismometers at the OAN-SPM given its proximity to the Mexicali valley, where many earthquakes do occur. A detailed geotechnical study of the TSPM site, including a site specific seismic hazard analysis, was done based upon extensive field studies discussed above.

The site specific seismic hazard analysis used both probabilistic and deterministic methodologies. In this particular case, the results did not differ much. The resulting design spectrum is presented

graphically in Figure 34 and its mathematical description is given in Table 8. Note that the accelerations in Figure 34 are not the ground accelerations expected in a maximum expected earthquake, but the response of single-degree-of-freedom oscillators to the ground accelerations (as a time series) from such an event. The time intervals 0-0.5 Hz, 0.5-2.0 Hz, and > 2 Hz correspond to the frequency intervals where ground acceleration, ground velocity, and ground displacement, respectively, are expected to dominate. Figure 35 presents three of the (many) time series used to generate the seismic design spectrum for the 975 year return period in Figure 34. The accelerations shown in Figure 35 are the horizontal ground accelerations. The vertical accelerations are assumed to be about 2/3 of the horizontal accelerations.

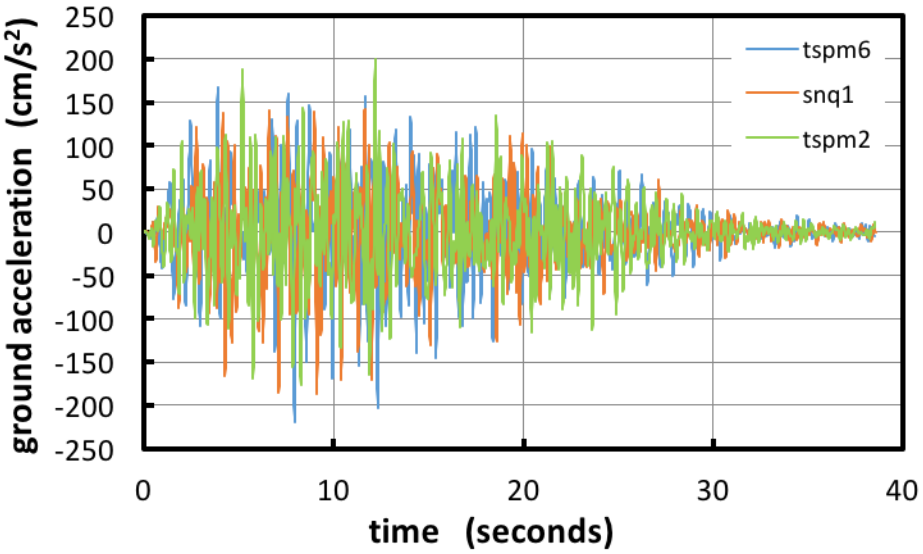

Figure 35: This figure presents three of the time series used to generate the 975 year design spectrum in Figure 34. The data required to generate this figure was provided by the GEIC-CFE.

9. ACKNOWLEDGEMENTS

Michael Richer thanks Urania Ceseña, María Herlinda Pedrayes, Enrique Colorado, Jesús González, Ignacio Manuel González Vidaurrazaga†, Eduardo López, Esteban Luna, Marco Moreno, José Manuel Murillo, Raúl Michel Murillo, Juan Manuel Núñez, Natalia del Pilar Parra Piedrahita, María Dolores González Mellado, Mauricio Reyes, Beatriz Sánchez, William Schuster, Gerardo Sierra Díaz, Mauricio Tapia, David Urdaibay, and Alan Watson for providing comments or information that is included in this document or helping to obtain or compile information used in this document.